

# Convection-permitting Modeling Strategies for Simulating Extreme Rainfall Events Over Southeastern South America

Martín Feijóo (✉ [martin.feijoo@cima.fcen.uba.ar](mailto:martin.feijoo@cima.fcen.uba.ar))

Centro de Investigaciones del Mar y la Atmosfera <https://orcid.org/0000-0001-5343-3609>

Silvina Solman

CIMA: Centro de Investigaciones del Mar y la Atmosfera

---

## Research Article

**Keywords:** extreme rainfall , convection-permitting modeling , Southeastern South America , domain configuration

**Posted Date:** July 24th, 2021

**DOI:** <https://doi.org/10.21203/rs.3.rs-675470/v1>

**License:**  This work is licensed under a Creative Commons Attribution 4.0 International License.

[Read Full License](#)

---

**Version of Record:** A version of this preprint was published at Climate Dynamics on March 12th, 2022.  
See the published version at <https://doi.org/10.1007/s00382-022-06226-z>.

---

# Convection-permitting modeling strategies for simulating extreme rainfall events over Southeastern South America

M. Feijoó · S. Solman

Received: date / Accepted: date

**Abstract** A set of six convection-permitting (CP) domain configurations were implemented to perform 72-hour long simulations of three extreme precipitation events over Southeastern South America (SESA). The goal of the study is to determine the most adequate configuration for reproducing not only the rainfall evolution and intensity, but also the synoptic triggering mechanisms that led to these extreme events, taking into account the trade-off between model performance and computational cost. This study assesses the impact of 1) the horizontal resolution in the CP domain, 2) the horizontal resolution of the driver domain, 3) the size of both CP and driver domains and 4) the nesting strategy (one-step versus two-step nesting). Each simulation was performed with the Weather Research and Forecasting model driven by the ERA-Interim reanalysis. For each event and

---

M. Feijoó

Universidad de Buenos Aires, Facultad de Ciencias Exactas y Naturales. Buenos Aires, Argentina.

Centro de Investigaciones del Mar y la Atmósfera (CIMA). CONICET – Universidad de Buenos Aires. Buenos Aires, Argentina.

Instituto Franco-Argentino para el Estudio del Clima y sus Impactos (IRL 3351 IFAECI). CNRS – IRD – CONICET – UBA. Buenos Aires, Argentina.

E-mail: martin.feijoo@cima.fcen.uba.ar

S. Solman

Centro de Investigaciones del Mar y la Atmósfera (CIMA). CONICET – Universidad de Buenos Aires. Buenos Aires, Argentina.

Instituto Franco-Argentino para el Estudio del Clima y sus Impactos (IRL 3351 IFAECI). CNRS – IRD – CONICET – UBA. Buenos Aires, Argentina.

Universidad de Buenos Aires, Facultad de Ciencias Exactas y Naturales, Departamento de Ciencias de la Atmósfera y los Océanos. Buenos Aires, Argentina.

18 domain configuration, a 6-member physics ensemble is built, making a total of 36  
19 simulations for each event. No significant differences were found between the 4 km  
20 and 2.4 km CP ensembles. Increasing the horizontal resolution of the driver do-  
21 main from 20 km to 12 km introduced only subtle differences. Increasing the size  
22 of the CP domain improved significantly the model performance, mainly because  
23 of better resolved topography and, hence, better resolved synoptic environment.  
24 The results in this study reveal that the one-step nesting CP ensemble at 4 km  
25 horizontal resolution covering an area of  $21^{\circ}\times 29^{\circ}$  (lat-lon) arises as the optimal  
26 domain configuration to simulate extreme precipitation events over SESA.

27 **Keywords** extreme rainfall · convection-permitting modeling · Southeastern  
28 South America · domain configuration

29 **Acknowledgements** This study has been supported UBACYT2018 Grant 20020170100117BA  
30 and FONCYT Grant PICT2018-02496.

31 **Declarations**

32 **Funding**

33 This study has been supported UBACYT2018 Grant 20020170100117BA and  
34 FONCYT Grant PICT2018-02496.

35 **Conflict of interest/Competing interest**

36 Not applicable

37 **Availability of data and material**

38 Not applicable

---

Code availability 39

Not applicable 40

Authors' contributions 41

All authors included in the authors list have contributed on different aspects of  
the manuscript. 42  
43

## 1 Introduction 44

Southeastern South America (SESA) hosts some of the most extreme convective 45  
storms of the planet (Zipser et al, 2006), accounting for more than 70% of the 46  
total extended summer precipitation in the region (Rasmussen et al, 2016). This 47  
certainly makes extreme precipitation events of critical relevance, not only be- 48  
cause of the high vulnerability of the population and the socio-economic activities 49  
(Vörösmarty et al, 2013), but also given that extreme precipitation has been in- 50  
creasing in frequency and intensity during the last decades (Penalba and Robledo, 51  
2010; Cerón et al, 2020; Olmo et al, 2020). Additionally, the frequency and inten- 52  
sity of these events are expected to continue increasing in response to the future 53  
global warming, as revealed in several studies based on either global climate mod- 54  
els (GCMs) or regional climate models (RCMs) (Chou et al, 2014; Blazquez and 55  
Solman, 2020). 56

Though several studies have demonstrated the added value of RCMs in repro- 57  
ducing regional scale phenomena and precipitation-related features over several 58  
areas of the world (Torma et al 2015 for Europe; Falco et al 2019 and Solman 59  
and Blazquez 2019 for South America, among others), RCMs are still deficient in 60  
reproducing extreme precipitation features mostly related with the limitations of 61  
the convective schemes (Prein et al, 2015). Particularly over SESA, RCMs have 62  
deficiencies in reproducing the intensity of extreme rainfall events and the exten- 63  
sion of the region where the most intense events occur (e.g. Solman et al, 2013; 64

65 Solman, 2016; Solman and Blazquez, 2019; Olmo and Bettolli, 2021, among oth-  
66 ers). Hence, there is an urgent need for implementing new modelling strategies to  
67 improve the capability of reproducing one of the most important climatic features  
68 in the region.

69 Advances in computational development allowed the implementation of models  
70 operating at convection-permitting (CP) resolutions, of the order of a few kilome-  
71 ters (Prein et al, 2015, 2020b, and references therein). Several studies showed  
72 that CP models (CPMs) outperform coarser RCMs in terms of their capacity in  
73 capturing the diurnal cycle of convective summer precipitation, the intensity of  
74 extreme precipitation events and orography-triggered convection (Matsudo et al,  
75 2015; Prein et al, 2013; Mahoney et al, 2012; Kendon et al, 2012). In early stages,  
76 these simulations were developed in the framework of the numerical weather pre-  
77 diction, in which simulations were performed for a few days covering the devel-  
78 opment of a specific event (e.g. Mahoney et al, 2012). More recently, CP climatic  
79 simulations covering a decade or more have been performed over different regions  
80 within Europe (e.g. Ban et al, 2020; Berthou et al, 2020; Kendon et al, 2012) and  
81 North America (e.g. Prein et al, 2020a). These studies highlight the benefits of  
82 CPMs in representing extreme precipitation features. CPMs have also been used  
83 to explore how extreme rainfall may change under future warming scenarios (e.g.  
84 Kendon et al, 2014, 2016; Fosser et al, 2016; Ban et al, 2015; Rasmussen et al, 2020)  
85 showing that these models project larger increases in extreme rainfall compared  
86 with coarser models. Due to the high computational cost of CP climatic simula-  
87 tions, most CP modelling exercises have been largely based on a single modelling  
88 approach. Only recently a coordinated effort based on decade-long multi-CP model  
89 simulations started to emerge mostly for domains over Europe (e.g. Coppola et al,  
90 2020; Ban et al, 2021; Pichelli et al, 2021).

91 Given the computational demand for performing ensemble simulations for a  
92 decade or more with CPMs, studies based on multiple CPMs simulating shorter  
93 periods, centered on single extreme precipitation events or on a single rainy season,

also emerged over several regions of the world, including Europe, North America, 94  
Asia and Africa (e.g. Pall et al, 2017; Hibino et al, 2018; Coppola et al, 2020; Li 95  
et al, 2019, 2018; Yang et al, 2017; Matsui et al, 2020). For South America, there 96  
are only some preliminary studies, (e.g. Lavín Gullón et al, 2021; Bettolli et al, 97  
2021; Solman et al, 2021), that highlight the benefits of CP models in capturing 98  
the main features of individual extreme events and their synoptic forcings. The 99  
studies by Lavín Gullón et al (2021) and Bettolli et al (2021) arose as a collabora- 100  
tive effort in the context of a CORDEX Flagship pilot study (<https://cordex.org/>) 101  
which produced a 6 month-length simulation performed with two CP RCMs, al- 102  
lowing for exploring model uncertainty in capturing selected extreme events, while 103  
Solman et al (2021) assessed the quality of a single model operating at CP res- 104  
olution in capturing the main features of a collection of extreme precipitation 105  
events in a single event approach. The domain of CP simulations in these studies 106  
spanned roughly  $12^\circ \times 12^\circ$  degrees with approximately  $350 \times 350$  grid points and 107  
were performed in a two-step nesting approach, with the CPM operating at 4km 108  
resolution, nested into a 20km-resolution domain. The results arising from these 109  
experiments showed that though the CP domain covered a large part of the re- 110  
gion where extreme events developed, several events fell too close to the lateral 111  
boundaries, suggesting that a larger CPM domain may be more adequate. Further- 112  
more, the two-step nesting approach introduced some deviations in the low-level 113  
circulation as a result of convective processes occurring close to the boundaries 114  
of the CP domain, modulating the main synoptic drivers of the events developing 115  
within the CPM domain. As discussed in Brisson et al (2015) both the nesting 116  
strategy and the domain size represent two key elements in the design of CPM 117  
simulations, with important consequences in both the quality and the computa- 118  
tional cost of the simulations. Though studies assessing the sensitivity of CPM 119  
simulations to domain size are quite a few, it is recommended that the domain 120  
size should be large enough to allow for a spatial spin-up of barely 150km (Brisson 121  
et al, 2015). However, an exceedingly large domain can generate deviations from 122

123 the lateral boundary conditions (LBC) and have undesired effects in the outflow  
124 boundary (Prein et al, 2015). Moreover, given the control of the synoptic drivers  
125 on the development of organized convection in SESA (Lavín Gullón et al, 2021;  
126 Solman et al, 2021, among others), the domain size in CPMs in the region should  
127 be large enough so that the forcing mechanisms driving to the occurrence of ex-  
128 treme rainfall events, often modulated by topographic features, are included in the  
129 domain.

130 The nesting strategy is another important source of model uncertainty and  
131 impacts on the computational cost of a CPM simulation as well. Most of the  
132 studies based on CPM simulations are performed using either three-step nesting  
133 in a telescoping mode (e.g. Fosser et al, 2014), two-step nesting (e.g. Ban et al,  
134 2021) or one-step nesting in which the CPM is driven by the reanalysis (e.g.  
135 Berthou et al 2020 for an European domain; Yun et al 2020 for a domain centered  
136 in eastern China; Liu et al 2017 for a domain over North America, among others).  
137 As discussed in Brisson et al (2015) multiple nestings may deteriorate the quality  
138 of a CPM simulation. On the other hand, in a one-step nesting approach, the  
139 resolution jump between the model providing the initial and lateral boundary  
140 conditions and the CP model impacts on the spatial spin-up, i.e, the distance  
141 from the boundaries of the CP domain that should be discarded (Matte and Lucas-  
142 Picher, 2017). Therefore, a sensitivity analysis to the nesting configuration needs  
143 to be performed to find the optimum CPM configuration for the SESA region.

144 Finally, the horizontal resolution in the CPM simulations is another key aspect  
145 to consider. CPM simulations operate at km-scale resolutions, from 4km (the upper  
146 limit for convection permitting simulations) to roughly 2km. However, the benefits  
147 of higher resolution in the CPM simulations are not fully explored. Considering  
148 that the choice of the spatial resolution also impacts on the computational cost of  
149 a simulation, a sensitivity analysis of the extent to which higher resolution implies  
150 better model performance needs to be tackled.

151 A careful design of CPM simulations, including the domain location, domain  
size, the spatial resolution and the nesting strategy should be considered to iden- 152  
tify the optimal model configuration that allows, on one hand, capturing the ex- 153  
treme precipitation events of a given region and the mechanisms that contribute 154  
to trigger, develop and sustain the deep moist organized convection and, on the 155  
other hand, accounting for the tradeoff with computational costs. The experimen- 156  
tal design described below will allow answering specific questions such as: Does 157  
the resolution of the driving model matters? Is there any significant improvement 158  
when increasing the resolution of the CPM simulations? Does the nesting strat- 159  
egy affect the quality of the CPM simulation? Does the domain size of the CPM 160  
simulation have an impact on the ability of capturing the evolution of an extreme 161  
event? 162

The goal of this study is identifying the optimal modelling strategy for perform- 163  
ing computationally feasible CPM simulations able to represent the main features 164  
of the extreme precipitation in SESA. Given the key forcing mechanisms leading 165  
to the formation of organized convection and subsequent extreme precipitation 166  
over SESA, including the northerly wind channeled by the Andes favoring mois- 167  
ture and heat flux together with a midlevel trough located over the Andes and an 168  
upper level jet stream with its associated upper level divergence (Rasmussen and 169  
Houze, 2016, and references therein), it is important to explore the extent to which 170  
including these forcing mechanisms within the CPM domain translate in a good 171  
representation of extreme events. With this aim, a series of short-term simulations 172  
have been performed with the WRF RCM (version 3.9.1; Skamarock et al, 2008) 173  
for a variety of domain sizes, horizontal resolutions and nesting strategies for a 174  
set of individual extreme precipitation events registered in SESA. The individ- 175  
ual event approach (Solman et al, 2021) allows for exploring the capability of the 176  
model in capturing the event but also exploring if the model is able to capture the 177  
corresponding triggering mechanisms. Identifying a CPM set up with a good per- 178

179 formance and with the lowest computational cost is needed before starting longer  
180 term simulations in the region.

181 The manuscript is organized as follows. In section 2 the datasets used for model  
182 validation together with the description of the model used, the experiment design  
183 and the metrics defined to assess model performance are described. In section 3  
184 the results of the capability of the model in reproducing the selected events for  
185 the variety of model configurations and nesting strategies is described. The focus  
186 of the evaluation is on the main features of the extreme rainfall event and the  
187 synoptic forcing mechanisms. Finally, in section 4 a summary of the main results  
188 and a discussion is presented.

## 189 **2 Data and methods**

### 190 **2.1 Datasets for validation**

191 For precipitation validation, three satellite precipitation estimates are used: the  
192 NOAA’s Climate Prediction Center Morphing Technique bias-corrected product  
193 (Joyce et al, 2004, CMORPH), the Global Precipitation Measurement Mission In-  
194 tegrated Multisatellite Retrievals calibrated precipitation Level-3 Final Run (Huff-  
195 man et al, 2019, IMERG) and the Multi-Source Weighted-Ensemble Precipitation  
196 V2.1 estimate dataset (MSWEP) described in Beck et al (2018). These datasets  
197 are based on integrating different types of satellite and ground station data. Some  
198 studies using CMORPH over SESA have reported wet biases in both extreme and  
199 weak precipitation (e.g. Salio et al, 2014; Matsudo et al, 2015; Demaria et al, 2011).  
200 Similar biases as those found for CMORPH were found for IMERG data by Cui  
201 et al (2019) but in assessing rainfall associated with mesoscale convective systems  
(MCSs) over the great plains in the USA. MSWEP merges gauge, satellite and 202  
reanalysis products and has been shown it has a good performance in monthly 203  
and seasonal scales over several regions of the world (Beck et al, 2017). Table 1 204  
lists information on the spatial and temporal resolution of the selected datasets. 205

Dataset	Temporal resolution (hs)	Spatial resolution
CMORPH	0.5	0.0727°
IMERG	0.5	0.1°
MSWEP	3	0.1°

**Table 1** Datasets used for the evaluation of the extreme precipitation events.

The ERA-Interim reanalysis at  $0.75^\circ \times 0.75^\circ$  spatial resolution (Dee et al, 2011) dataset was used to provide the initial and lateral boundary conditions for the simulations described in Sect. 2.3. For evaluating the model performance in terms of the triggering circulation patterns for individual extreme precipitation events, both the ERA-Interim reanalysis and the ERA5 reanalysis (Hersbach et al, 2020) were used. ERA5 was included in the evaluation in order to compare the modelled circulation features against a reanalysis dataset operating at higher resolution (roughly 31 km) and with better performance, compared with driving ERA-Interim reanalysis.

## 2.2 Event selection

Daily rainfall data from the gridded Tropical Rainfall Measurement Mission (TRMM) 3B42 V7 (Huffman et al, 2011) dataset for the period 2000 to 2017 was used to identify the extreme rainfall events. First, the 95<sup>th</sup> percentile of rainy days (rainfall above 1 mm/day) was computed for every grid point within the SESA region. Extreme precipitation at a given day is defined when precipitation is above the 95<sup>th</sup> percentile at a given grid point and at adjacent grid points within a region of  $1.25^\circ \times 1.25^\circ$  size. These criteria allowed identifying extreme events with a minimum spatial extension accounting for organized convection in the region. After applying these criteria, three extreme events were selected. A detailed description of the events can be found in section 3.1.

Member	1	2	3	4	5	6
MP	WDM6	WDM6	WDM6	WDM6	WSM6	WDM6
Cumulus	KF	KF	KF	KF	GF	KF
PBL	MJY	YSU	YSU	MYNN3	MYNN3	MYNN3
ShCu	-	-	GRIMS	-	GRIMS	GRIMS
LW Rad	Dudhia	Dudhia	Dudhia	Dudhia	Dudhia	Dudhia
SW Rad	RRTM	RRTM	RRTM	RRTM	RRTM	RRTM
SfcLay	ETA S	Rev. MM5	Rev. MM5	ETA S	ETA S	ETA S
Land	UNOAH	UNOAH	UNOAH	UNOAH	UNOAH	UNOAH

**Table 2** Selection of physics schemes used for each member of the physics ensemble. Cumulus parameterization in the CP domains is turned off. Acronyms used: *MP*: Microphysics scheme, *PBL*: Planet boundary layer scheme, *ShCu*: Shallow cumulus scheme, *LW Rad/SW Rad*: Longwave and Shortwave radiation scheme, *SfcLay*: Surface Layer scheme, *Land*: Land Surface scheme. WDM6/WSM6: Lim and Hong (2010); KF: Kain (2004); GF: Grell and Freitas (2014); MJY: Janjic (1994); YSU: Hong et al (2006); MYNN3: Nakanishi and Niino (2009); GRIMS: Hong and Jang (2018); Dudhia: Dudhia (1989); RRTM: Mlawer et al (1997); ETA S: Janjic (2002); Rev MM5: Jimenez et al (2012); UNOAH: Tewari et al (2016).

### 2.3 The WRF model and experimental design

226

The Weather Research and Forecast model (WRF; Skamarock et al, 2008) version

227

3.9.1 was used in this study to perform short-term (72-hour) simulations for the

228

selected extreme events. For each event, the model was initialized at 00 UTC of

229

the day before the occurrence of the extreme event, being the first 6 hours of the

230

simulations considered as spin-up time and, therefore, discarded for the analysis.

231

Both initial and lateral boundary conditions (LBC) were provided by the 0.75°

232

horizontal resolution ERA-Interim reanalysis. All simulations were performed with

233

39 vertical levels. The relaxation zone at the boundaries has an extension of around

234

0.75°.

235

For each event and for each model configuration, a physics ensemble was built

236

to account for model uncertainty. The members of the physics ensemble differ

237

mainly in the cumulus, microphysics, planetary boundary layer and shallow convec-

238

tion parameterizations. The physics ensemble comprises 6 members, as described

239

in Table 2. The analysis of the CPM simulations described below is based on the

240

physics ensemble mean.

241

		DR		CP			
	$\Delta x$	no. of pts	Lon range Lat range	$\Delta x$	no. of pts	Lon range Lat range	Name
D1	12 km	52192	76°W , 46°W 43°S , 19°S	2.4 km	300696	66°W , 53°W 37°S , 25°S	CP1-2.4(12)
		”	”	4 km	103648	”	CP1-4(12)
D2	12 km	154280	87°W , 37°W 47°S , 7°S	4 km	279220	77°W , 52°W 39°S , 23°S	CP2-4(12)
	20 km	55404	”	4 km	”	”	CP2-4(20)
	-	-	-	4 km	”	”	CP2-4
D3	-	-	-	4 km	426960	77°W , 48°W 36°S , 15°S	CP3-4

**Table 3** Summary of the experimental set-up including the domain name, the horizontal resolution ( $\Delta x$ ), the number of gridpoints (no. of pts), the spatial coverage and the name of the CP simulations. DR denotes the driving domain and CP denotes the convection-permitting domain.

242 The three selected events were simulated using a set of different domain con-  
243 figurations, including different nesting strategies (two-steps nesting vs one-step  
244 nesting), different domain sizes for both the two domains in the two-step nesting  
245 approach and the single domain for the one-step nesting approach, and different  
246 spatial resolutions (including the spatial resolution of the outer domain in the  
247 two-step nesting approach and the CPM domain). This experimental setup in-  
248 cludes three domain sizes referred to as D1, D2 and D3. For each domain size,  
249 the two-step nesting includes the outer domain driven by the reanalysis, referred  
250 to as the driving domain (DR) which provides the lateral boundary conditions to  
251 a smaller domain at convection-permitting resolution (CP), corresponding to the  
252 CP domain. Accordingly, the difference in the physics choices between DR and CP  
253 domains is that the convective scheme is switched on or off, respectively. Figure 1  
254 shows the driving and the convection-permitting-resolution domains for the three  
255 domain sizes and Table 3 summarizes the description of the simulations. Consid-  
256 ering all combinations displayed in Tables 1 and 3, a total of 36 simulations have  
257 been performed for each individual event, with 6 ensemble members for 6 different  
258 model set-ups.

259 Simulations performed at D1 include the DR1 domain with a horizontal reso-  
260 lution of 12 km (roughly 50K grid points) and the CP1 domain at two horizontal  
261 resolutions: 2.4 km (roughly 300K grid points) and 4km (roughly 100K grid points),

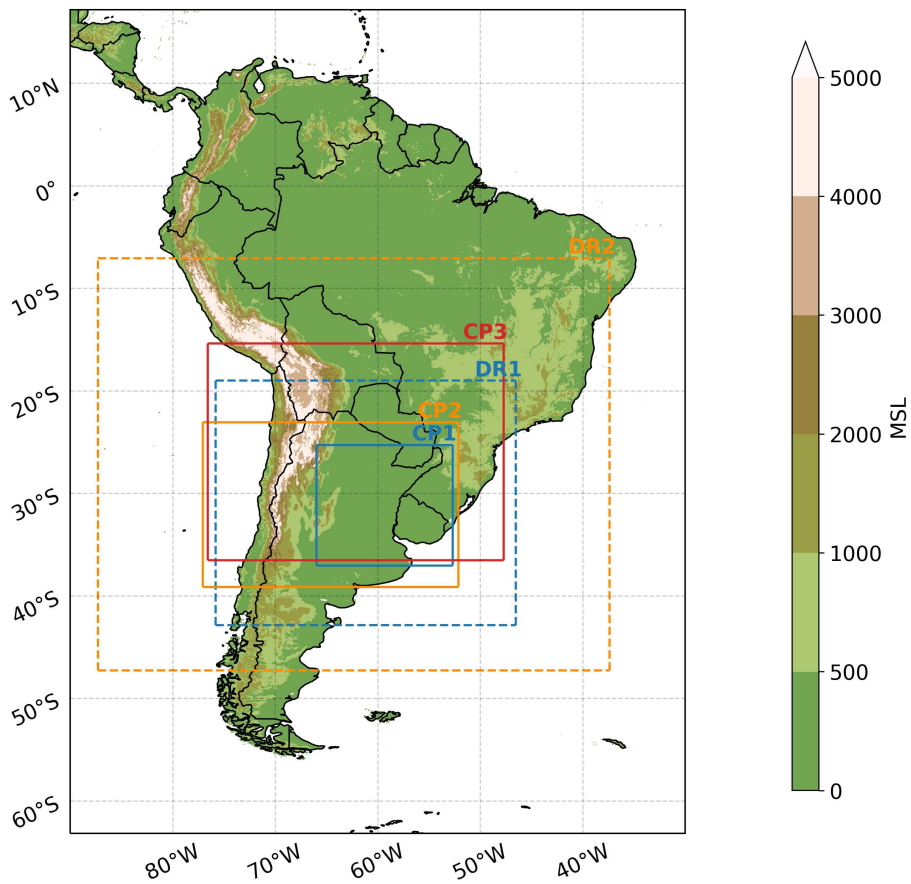


**Fig. 1** Domain configurations of the WRF 3.9.1 simulations. Blue, orange and red squares indicate domains D1, D2 and D3, respectively. Dashed lines indicate the driving domain (DR) in the two-step nesting approach. Solid lines indicate the domain of the convection – permitting (CP) simulations

262 respectively. These CP simulations allow exploring to which extent the horizon-  
 263 tal resolution of the CP domain matters. The CP1 simulations cover an area of  
 264 approximately  $13^\circ \times 12^\circ$  (longitude - latitude). Simulations performed at D2 differ  
 265 from D1 in the size of the domain and also in the nesting strategy. For the two-  
 266 step nesting configuration, not only the DR2 domain extends over a much broader  
 267 area compared with DR1 allowing for a better representation of the large scale  
 268 forcings entering the CP domain, but the western boundary of the CP2 simulation  
 269 is located off the coast of Chile and hence, allowing for a proper interaction be-

270 tween the inflow at that boundary and the complex Andes topography. Moreover,  
271 the CP2 domain includes the Sierras de Córdoba over central Argentina where  
272 convection usually starts (Rasmussen et al, 2016). Given the dominant role of the  
273 Andes in modulating the westerly flow and given the control that the Sierras de  
274 Córdoba exert on the triggering mechanisms for convective processes to initiate,  
275 this domain configuration allows exploring the relevance of including the main  
276 topographic features controlling the mechanisms associated with the occurrence  
of organized convection in SESA. The CP2 domain is implemented only at 4 km 277  
horizontal resolution, with roughly 280K grid points and covers an area of ap- 278  
proximately  $25^{\circ} \times 16^{\circ}$ . In order to explore the impact of the horizontal resolution 279  
in the two-step nesting configuration, DR2 was implemented at two horizontal 280  
resolutions, 12 km and 20 km, corresponding to barely 150K and 55K grid points. 281  
Additionally, one of the physics ensembles performed in the CP2 domain is driven 282  
directly by the ERA-Interim reanalysis, hereafter referred to as the one-step nest- 283  
ing configuration. This experiment is designed to explore the nesting strategy, i.e. 284  
two-step vs. one-step nesting. This last set up also rises the issue of the spatial 285  
spin-up, since the resolution rate between the model providing the lateral bound- 286  
ary conditions (LBC) and the CP domain is close to 18 and hence, a large number 287  
of grid points close to the boundaries needs to be discarded to avoid introducing 288  
noise due to the resolution jump. 289

Finally, D3 is configured in a one-step nesting approach, similarly as one of 290  
the experiments in the D2 set up, but with a larger domain, spanning  $29^{\circ} \times 21^{\circ}$ . 291  
The aim of exploring this domain is to enlarge the CP domain in order to capture 292  
not only the extreme events but also the circulation driving the evolution of the 293  
events. Note that the CP3 domain is not only larger than the CP2 configured in 294  
the one-step nesting approach, but its northern boundary is located up to  $15^{\circ} \text{S}$ , 295  
allowing for better capturing the low-level northerly moisture flow -a key ingredient 296  
to develop deep convection. 297

The experimental set up described above is also framed considering the trade-offs between domain configuration, including domain size, resolution and nesting strategy, and computational costs. It is also worth recalling that the larger the number of nesting steps the more the computational cost of the simulations.

## 2.4 Metrics and Analysis

The focus of this study is on evaluating the extent to which different model configurations capture extreme precipitation events together with their triggering forcing mechanisms. Hence, the analysis is centered on the main features of three precipitation events in terms of their intensity, location and temporal evolution and on the low-level circulation patterns, namely, the meridional component of the wind and the geopotential field at 850hPa. Given the dominant role of the moisture flux convergence on the development of the extreme events over SESA (Lavín Gullón et al, 2021; Solman et al, 2021), the vertically integrated moisture flux for each of the selected events has also been evaluated. The analysis is focused on the low-level circulation since it is at the lower levels of the atmosphere where the regional forcings associated with topographical features may have the largest impact.

The skill of the models in representing the precipitation events is assessed with the Fractional Skill Score (FSS; Roberts and Lean, 2008). The FSS is a metric based on a neighborhood approach that measures how the simulation skill varies with the spatial scale at which simulations and observations are being compared. The FSS compares the observed and modeled fraction of grid points with precipitation above a certain threshold within a running square domain of varying size, ranging from a single grid cell to twice the size of the simulation domain. The FSS ranges from 0 to 1, being 1 a perfect skill. Roberts and Lean (2008) defined a critical FSS that indicates the minimum value of FSS that should be reached for a skilfull prediction. The FSS is generally monotonically increasing with the spatial scale, hence, the smaller the scale at which the FSS equals the skilfull scale, the

325 better the model performance, indicating that the model is able to capture the  
326 fractional precipitation occurring at smaller scales.

327 In order to account for the timing and intensity of the precipitation events, the  
328 FSS was calculated for each member of the ensemble against every observational  
329 dataset every 3 hours during the whole event. The minimum spatial scale at which  
330 the model is skillful is computed at each timestep. The precipitation threshold se-  
331 lected for the calculations of the FSS is the 95<sup>th</sup> spatial percentile of the observed  
3-hourly precipitation. Therefore, for each event, each ensemble member and each 332  
observational dataset, the minimum spatial scale was computed, and the distribu- 333  
tion of the minimum skillful scale for every set of CPM simulation is represented 334  
in a box-plot. 335

Due to the FSS compares observed and simulated precipitation, every simu- 336  
lation and observational dataset was bilinearly interpolated onto a common grid 337  
of  $0.1^\circ \times 0.1^\circ$ . This resolution corresponds to the lowest resolution among the ob- 338  
servational datasets. This interpolation implies an upscaling of the CPM simula- 339  
tions and, therefore, an apparent loss in high resolution information but it is still 340  
expected that high resolution information is transferred into the upscaled lower 341  
resolution domain (Torma et al, 2015; Fantini et al, 2018). This interpolation was 342  
also applied to adequately compare the synoptic and precipitation fields between 343  
the simulations and the datasets. 344

### 3 Results 345

In what follows an overview of the selected extreme precipitation events is pre- 346  
sented. Then, the performance of the ensemble mean CPM simulations correspond- 347  
ing to the 6 model configurations (listed in Table 2) is assessed for each event in 348  
terms of their capability in reproducing the spatial distribution of the maximum 349  
3-hourly accumulated precipitation, the temporal evolution of the 3-hourly accu- 350  
mulated precipitation during the onset, mature stage, and decay together with the 351  
associated circulation features. 352

	Case1 2005-03-12			Case2 2015-11-10			Case3 2016-10-24		
	CMORPH	IMERG	MSWEP	CMORPH	IMERG	MSWEP	CMORPH	IMERG	MSWEP
P90	74	70	69	59	36	34	54	47	38
P95	124	105	112	86	70	51	75	72	52
P99	213	158	143	111	122	70	110	116	72
A+50	26.4	22.4	20	18.8	11.3	7.8	16.5	13.2	8.1

**Table 4** Summary of the daily precipitation features of the selected individual events for each precipitation dataset. The three middle rows depict the spatial percentiles of the daily precipitation corresponding to the 90<sup>th</sup>, 95<sup>th</sup> and 99<sup>th</sup> (mm/day) and the bottom row displays the approximate extension of the area ( $\times 10^4 \text{km}^2$ ) where the daily precipitation is above 50 mm/day.

### 353 3.1 Description of the selected events

354 Table 4 lists the dates of the selected extreme events together with some specific  
355 features, such as extreme spatial percentiles of the daily precipitation and the area  
356 covered with precipitation above 50 mm/day as depicted by each of the datasets  
357 listed in Table 1. Case 1, occurring on March 12<sup>th</sup>, 2005, is the most intense event  
358 as denoted by the spatial 99<sup>th</sup> percentile of the daily rainfall ranging between 143  
359 mm/day to 213 mm/day, depending on the dataset. Inspection of the 3-hourly pre-  
360 cipitation of all datasets (not shown) revealed that the event initiated at around  
361 18 UTC on March 11<sup>th</sup> east of the Andes Mountain range, progressed eastwards  
362 reaching the peak precipitation at 06 UTC on March 12<sup>th</sup> and further propagating  
363 northeastward while acquiring a northeast-southwest band shape. This is the typ-  
364 ical behavior of MCS in SESA according to the literature (Rasmussen and Houze,  
2016; Matsudo and Salio, 2011; Romatschke and Houze, 2013). Figure 2 shows 365  
the 3-hourly peak precipitation for the Case 1 event. Satellite estimates (Fig. 2 a, 366  
d and g) display two maximums, with the largest peak rainfall ranging from 45 367  
mm to above 100 mm centered on 31°S 61°W and a secondary peak located to 368  
the northwest. The discrepancies among datasets in terms of the intensity of the 369  
peaks are remarkable. 370

Case 2 started at 18 UTC on November 9<sup>th</sup> 2015, progressed eastwards reaching 371  
the peak precipitation at 06 UTC on November 10<sup>th</sup> over northeastern Argentina 372  
close to the border with Brazil and propagated further eastward during its decline 373

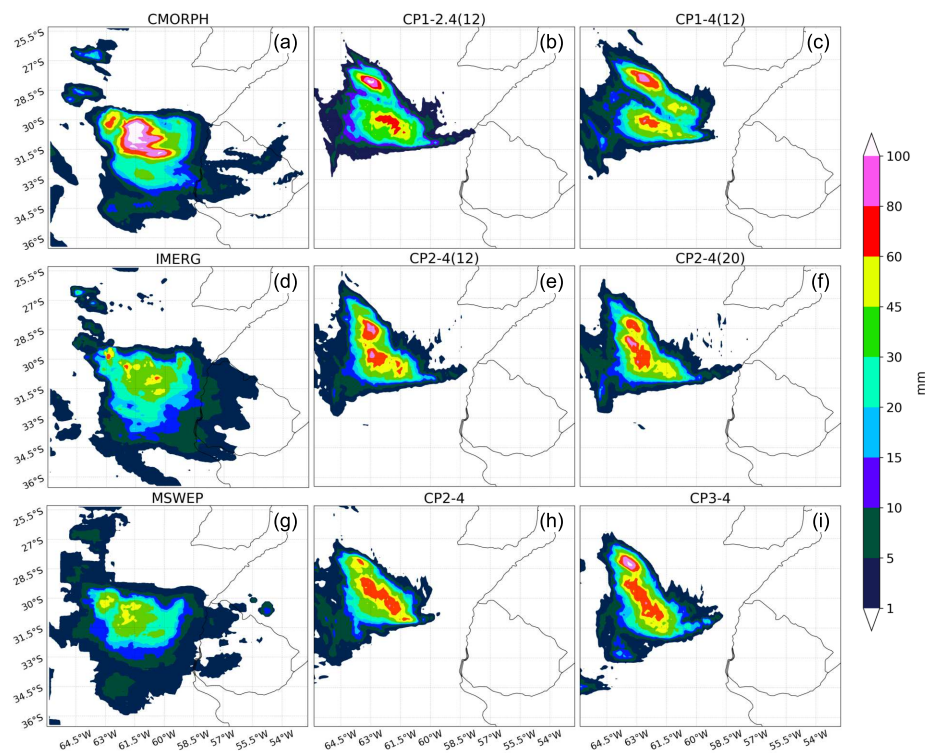


**Fig. 2** Maximum 3-hourly precipitation for Case 1 (mm). Left panels (a, d, g) display the observational datasets. Central and right panels display the ensemble mean of CPM simulations listed in Table 3.

(not shown). The spatial 99<sup>th</sup> percentile of the daily rainfall during the day of  
 374 maximum rainfall ranges from 70 to 111 mm/day, as depicted by the 3 datasets  
 375 (Table 4). Peak 3-hourly precipitation displayed in figure 3 shows that the peak  
 376 3-hourly rainfall (e.g. above 60 mm) is very localized over a small region centered  
 377 at roughly 28.5°S 56°W, though the area with heavy rainfall extends over a much  
 378 broader region, as depicted by every dataset. A less intense precipitation system  
 379 is also apparent to the southwest of the main peak. The agreement in the spatial  
 380 distribution of rainfall at the time of the maxima among the three datasets is  
 381 apparent.  
 382

383 Case 3 started during nighttime hours, around 00UTC and 03 UTC on October  
 384 24<sup>th</sup> 2016 and reached the peak precipitation intensity at 09 UTC on October  
 385 24<sup>th</sup>, being a more explosive event compared with Cases 1 and 2 (not shown). The

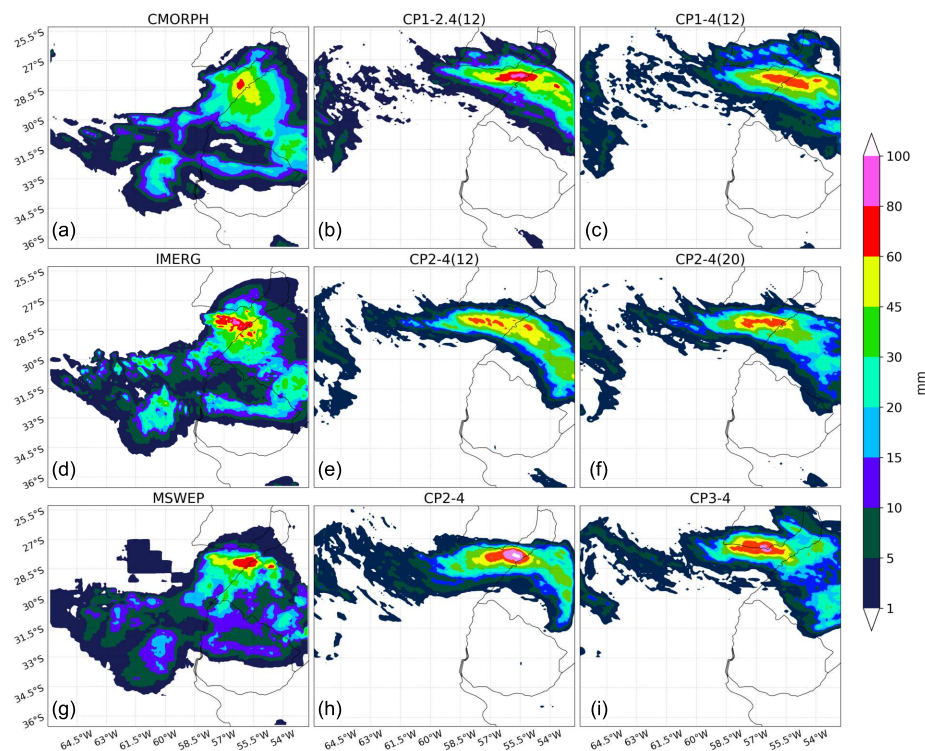


**Fig. 3** Same as Fig. 2 but for Case 2.

386 maximum 3-hourly rainfall for this event displayed in Figure 4 depicts a localized  
 387 area with peak intensity centered around 29°S, 59°W and a secondary peak further  
 388 to the west. Additionally, a secondary system developing over the southwestern  
 corner of the domain is also apparent. The observations encompass a wide range  
 389 of rainfall intensities at the time of the maximum peak, but every dataset agrees  
 390 on the location and spatial extent of the precipitation maximum. This event is  
 391 characterized by a much more localized system which may represent a challenge in  
 392 terms of model performance. A relevant feature of this event is that heavy rainfall  
 393 started at night hours (21hs to 00hs local time) while the other two events started  
 394 in the afternoon and reached the peak during early morning hours, in agreement  
 395 with the typical diurnal cycle of extreme rainfall events developing in the region  
 396 (Rasmussen et al, 2016).  
 397

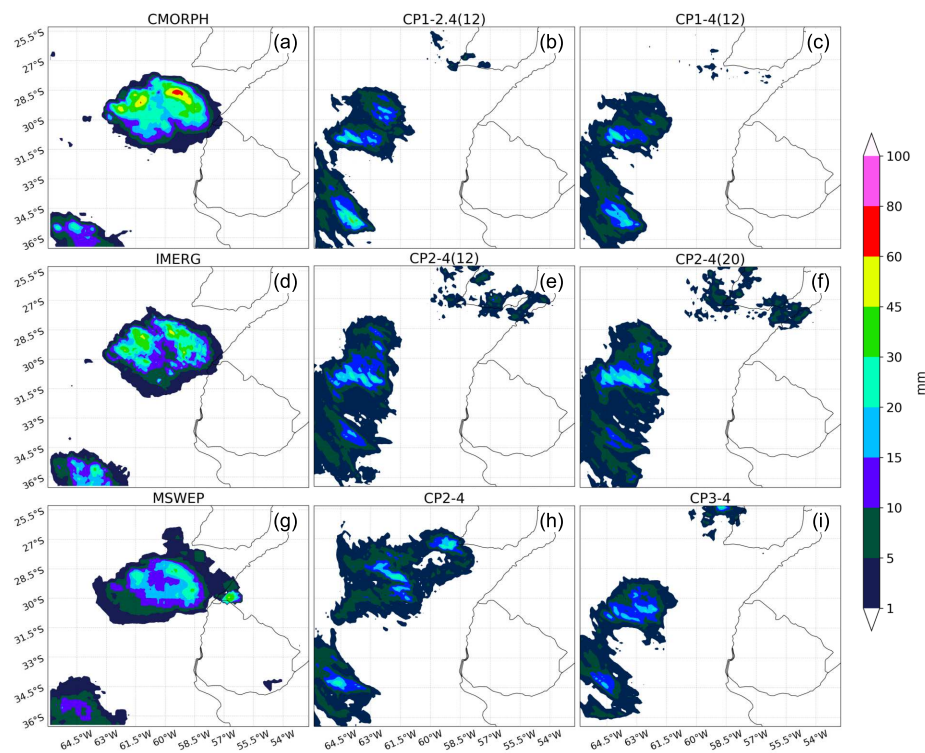


**Fig. 4** Same as Fig. 2 but for Case 3.

The discrepancies in the precipitation intensity among datasets for the three extreme events emerge clearly from Table 4 and figures 2, 3 and 4, with CMORPH showing the highest values and MSWEP showing the lowest values. The spread in the precipitation amount among datasets increases with the spatial percentile, revealing the difficulties of the satellite estimates to reproduce extreme precipitation. The observational uncertainty associated with extreme rainfall events arises clearly in this analysis. It represents a serious obstacle for assessing model performance, given that the assessment of model performance will strongly depend on the observational dataset used.

### 3.2 Simulated precipitation

407

A comparison of the peak 3-hourly accumulated precipitation between the set of CP experiments (Table 3) and observations for each individual event is displayed in Figures 2, 3 and 4, respectively.

408

409

410

For Case 1, Figure 2 shows that all CP simulations broadly capture the event, though there are some differences among the set of model configurations. First, all simulations display the core of the event slightly shifted towards the northwest compared with the observations. The maximum intensity is similarly represented by every CP simulation, but it is difficult to identify the extent to which the simulations are overestimating or underestimating the peak given that the maximum intensity from the set of observations is quite dissimilar. If we compare the two-step nesting simulations for the D1 domain, the 2.4km resolution ensemble CP1-2.4(12) against the 4 km resolution ensemble CP1-4(12), (Fig. 2b and c), the differences are quite subtle, suggesting that for this individual event the resolution of the CP model does not have a strong impact on the quality of simulated precipitation. Enlarging the domains (D2 vs D1) does not translate into any significant impact (Fig. 2c vs e), nor does the horizontal resolution of the driving domain (Fig. 2e vs f). The location and spatial extension of the system is sensitive to the nesting strategy (Fig. 2e vs h) though only for the larger CP domain (Fig. 2i) the system seems to be better reproduced. In this CP ensemble (CP3-4) the system extends to the southeast, in a better agreement with the observations, and the unrealistic rainfall close to the western boundary that is present in all the other CPM configurations, is not simulated.

411

412

413

414

415

416

417

418

419

420

421

422

423

424

425

426

427

428

429

For Case 2 (Fig. 3) every simulation captures the core of the peak precipitation in terms of both location and intensity, though the spatial extension of the system is restricted to a smaller area compared with the observations. No simulation reproduces the broader area with intense rainfall extending over the central part of the domain. The event develops too close to the eastern boundary in the CP domains D1 and D2, suggesting that these domains may be too small for simulating

430

431

432

433

434

435

436 extreme events in SESA that may develop over a broader area extending further  
437 east. Moreover, the one-step nesting ensemble over domain D3 (Fig. 3i), CP3-4,  
438 is the only simulation reproducing the secondary maximum rainfall over southern  
439 Brazil, though it still fails in capturing the overall rainfall spatial distribution.  
440 As was noted for Case 1, no remarkable differences are found between the 2.4km  
441 and the 4km resolution CP1 ensembles (Fig. 3b vs c). The peak rainfall seems to  
442 cover a smaller area for the CP2 ensembles compared with CP1, suggesting that  
443 enlarging the CP domain towards the west does not have a systematic impact on  
444 improving the quality of the simulated rainfall. Additionally, the one-step nesting  
445 over the D2 domain (CP2-4) does not display any important difference compared  
446 with the two-step nesting simulation (either CP2-4(12) or CP2-4(20)).

For Case 3 (Figure 4) every CP simulation fails in reproducing the core of the 447  
event at the right location, but a center of rainfall above 15 mm located further to 448  
the west, at 63°W, is apparent. Only the one-step nesting CP simulation over the 449  
D2 domain, CP2-4 (Figure 4h) reproduces a rainfall center in a better agreement 450  
with the observations. As for Cases 1 and 2, no differences can be highlighted 451  
between CP simulations at different resolutions. Results are sensitive to the size 452  
of the domain (e.g. D1 vs D2) though no improvement in the quality of the CP 453  
simulations is apparent in the two-step nesting experiments when a larger domain 454  
is used (middle row vs top row). 455

The misrepresentation of the peak precipitation for some of the selected events 456  
analyzed may be due to either the CP simulations fail in reproducing the event or 457  
they fail in reproducing its temporal evolution. In order to explore the capability of 458  
the CP simulations in reproducing the temporal evolution of the systems, Figures 459  
5 display the time-series of the spatially averaged 3-hourly accumulated rainfall. 460  
Large differences are found among the three different observational datasets, with 461  
CMORPH systematically overestimating IMERG and MSWEP datasets. Though 462  
there is an overall agreement on the temporal evolution of each event among the 463  
three datasets, CMORPH depicts some inconsistencies on the time of the day 464

of the precipitation peak, compared with IMERG and MSWEP. It is worth to recall that both IMERG and MSWEP are blended with station data, hence, they probably agree better with station data in terms of the timing of the events than CMORPH. All CP simulations adequately capture the onset, the peak and the decay of the three extreme events, with some subtle differences in the intensity of the maximum peak and to a lesser extent in the time of the day when the maximum rainfall is simulated. Overall, no systematic differences among the 6 CP ensembles are apparent. For Case 1, the development of a secondary system after the decay of the main event is apparent from the observations. However, the CP simulations produce a weaker event peaking three hour later. After the decay of the main event in Case 2, there is also a secondary system clearly identified in the observations from 00UTC to 18UTC on November 11<sup>th</sup> 2015. CP simulations can capture the evolution of this secondary system but there are large differences in terms of the timing of the peak intensity and in the rainfall intensity. Only the two-step nesting CPs over the D2 domain adequately captures the temporal evolution and the intensity of this event. For Case 3, all CP simulations underestimate the rainfall amount all along the lifecycle of the event and fail in capturing the time of the maximum peak. However, the evolution of the rainy system developing during the following day is well reproduced. Note that this event has a much smaller spatial scale compared with Cases 1 and 2 and hence, it may be more difficult to be adequately simulated.

Overall, the higher the spatial resolution in the CP simulations for domain D1 the larger the intensity of the peak rainfall, consistent with the literature (e.g. Li et al, 2019; Fosser et al, 2014). This is due to that higher resolution CP simulation produces more localized cells with larger precipitation intensity (not shown). The spread among members of each CP ensemble is systematically larger when the rainfall intensity is higher. Considering that the CP ensemble members differ in the microphysics schemes, the planetary boundary layer schemes and the treatment of the shallow convection, this is expected since the processes involved exert a

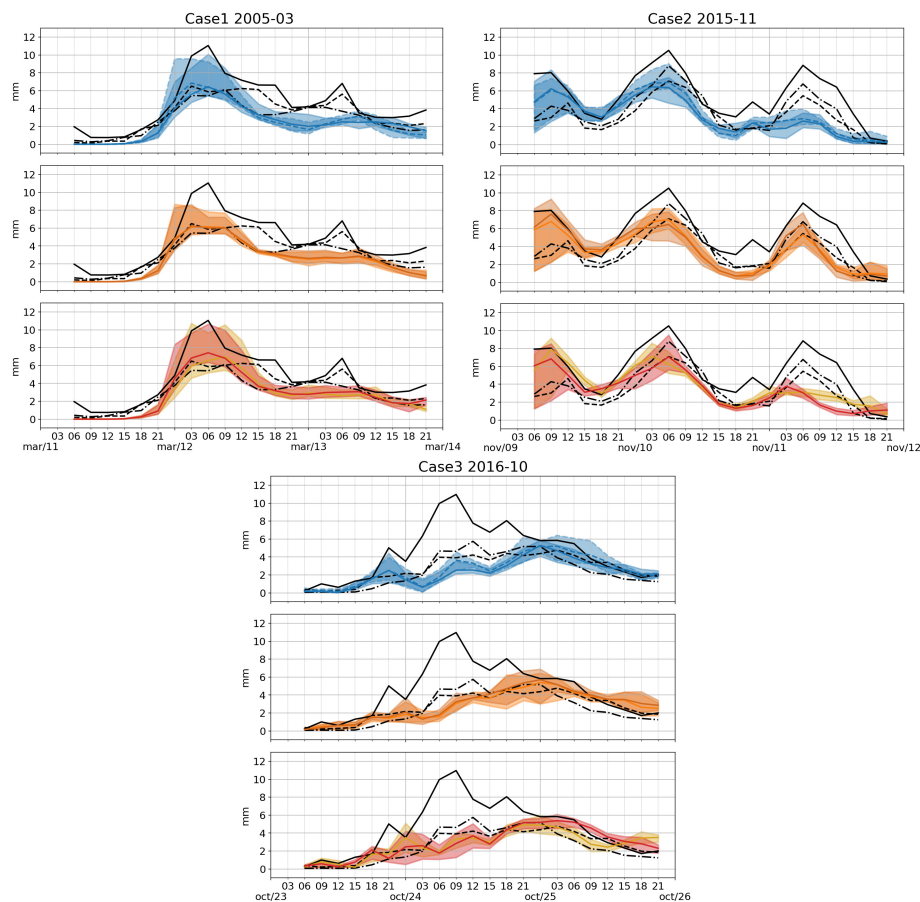


**Fig. 5** Time-series of the 3-hourly accumulated rainfall averaged over the target area for Case 1 (left column), Case 2 (central column) and Case 3 (right column). The ensemble mean (lines) and the ensemble spread among members of CP simulations (shaded) are displayed for the two-step nesting CP simulations at the D1 domain (top), the two-step nesting CP simulations at the D2 domain (middle) and the two one-step nesting simulations over D2 and D3 (bottom), respectively.

strong impact on how convection is triggered and on the hydrometeors, and hence, 494  
 on the rainfall produced. It is also worth highlighting that after the decay of the 495  
 496 core extreme event, the spread among members is lower for the one-step nesting  
 497 simulations. This feature is particularly important when considering CP simula-  
 498 tions covering longer periods, since reducing the uncertainty of the simulations is  
 499 a key challenge.

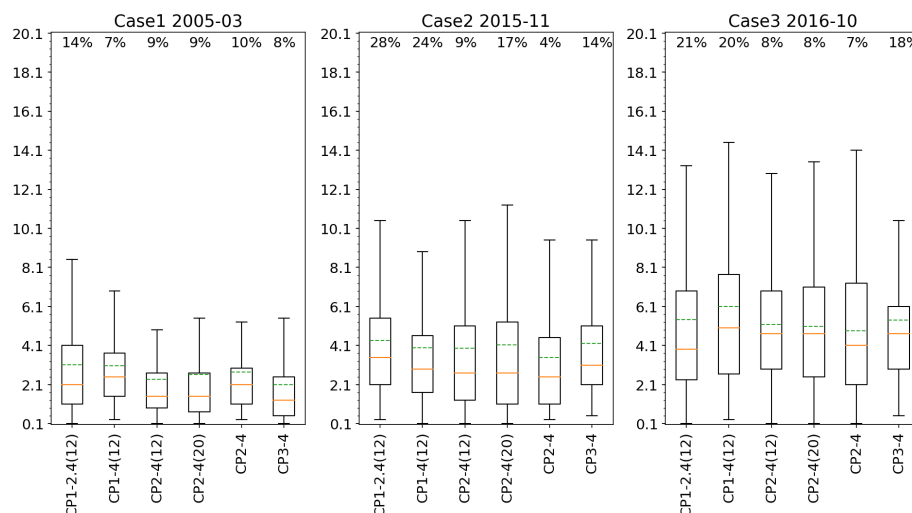


**Fig. 6** Boxplot of the minimum spatial scale at which each CP ensemble is skillful. The horizontal axis indicates the CP ensembles, and the vertical axis indicates the minimum spatial scale. The boxes and whiskers are built from the information derived from the FSS computed every 3 hours against each of the three observational datasets and for each of the 6 members of the ensemble. The numbers in the upper part of each boxplot represent the percentage of times in which the FSS score does not reach a skillful value. The orange and green lines indicate the 50th percentile and the mean value of the minimum spatial scales, respectively. The boxes delimit the 25th and 75th percentiles and the whiskers denote the 5th and 95th percentiles.

500 The evaluation based on the spatial distribution of the peak rainfall and on the  
 501 temporal evolution of the events is limited due to part of the information charac-  
 502 terizing the extreme events may be missing. It is important to assess the capability  
 503 of the CP simulations in capturing the timing, the intensity and the location where  
 504 precipitation occurs. Accordingly, and to provide a more quantitative measure of  
 505 the quality of the set of CP simulations, the FSS score is evaluated. The minimum  
 506 spatial scale at which the FSS reaches a skillful value is obtained along the life  
 507 cycle of each event for each ensemble member, computed against each of the three  
 508 observational datasets. Figure 6 shows a box-plot of the minimum skillful spatial  
 509 scale at which each simulation captures the fractional 3-hourly precipitation for  
 510 each event. The lower the spatial scale, the better the CPM performance.

511 As found in the previous analysis, increasing the spatial resolution of the CP  
 512 ensemble does not always imply better model performance. The 2.4 km resolution  
 513 CP1 ensemble does not display systematic smaller skillful spatial scales compared

514 with the 4km resolution CP1 ensemble nor displays systematic reduction of the  
515 ensemble spread. Moreover, the frequency at which the FSS does not reach a  
516 minimum skillful spatial scale is higher for the higher resolution CP1 ensemble.  
517 Hence, increasing the spatial resolution of the CP simulation does not necessarily  
518 implies better model performance. Accordingly, results for these three single events  
519 indicate that no added value is found when increasing the horizontal resolution  
520 from 4km to 2.4km. This is an important outcome given the impact of increasing  
521 resolution on the computational cost of the simulations. The spatial resolution  
of the driving domain does not impact on the capability of the CP ensemble in 522  
capturing the peak of the events. This result arises when comparing the 4km CP 523  
ensemble nested in either the 12km or the 20km driving model over the domain 524  
D2 (CP2-4(12) vs CP2-4(20)). Again, this outcome has important implications in 525  
terms of computational costs. However, when the size of the domain is enlarged 526  
(e.g., the 4km CP ensemble over D1 vs the 4km CP ensemble over D2), the CP 527  
ensemble displays smaller skillful spatial scales, suggesting that the domain size of 528  
the CP simulation does have an impact on the capability of the model in capturing 529  
the events. This is particularly evident for Cases 1 and 3. This is an expected result, 530  
given that the D2 nested simulations can better capture the triggering mechanisms 531  
associated with the topographic forcing compared with the CP ensemble in the 532  
D1 domain. Concerning the nesting strategy, the one-step nesting displays a clear 533  
improvement compared with the two-step nesting for Cases 2 and 3 in terms of 534  
reducing the skillful spatial scales (e.g., comparing the 4km CP ensemble driven by 535  
either the 12km or the 20km resolution RCM, referred to as CP2-4(12) and CP2- 536  
4(20), vs the 4km CP ensemble driven by the reanalysis, referred to as CP2-4). 537  
Enlarging the CP domain in the one-step nesting approach translates in a better 538  
model performance, particularly for Case 1. For Cases 2 and 3 the CP3-4 ensemble 539  
displays a smaller spread among ensemble members. Furthermore, given that one- 540  
step nesting simulations involve only one domain, in terms of computational costs 541  
they result cheaper than the two-step nesting approach. In fact, comparing the 542

computational resources used to perform the CP2-4 (12) simulations against the CP2-4 simulations, the latter was roughly 30% cheaper.

### 3.3 Synoptic forcings

As already mentioned earlier, extreme precipitation events in SESA are mostly associated with organized deep moist convection (Rasmussen et al, 2016). Isolated convective cells usually initiate during the afternoon hours on the east side of the Andes and the Sierras de Córdoba hills located over central Argentina. These systems propagate further eastward and develop into organized convective systems in the presence of the South American low-level Jet (SALLJ). The SALLJ is a northerly wind that advects warm moist air from the Amazon forest into subtropical latitudes (Salio et al, 2007). The SALLJ penetration into higher latitudes together with a mid-to-upper-level subsidence in the lee side of the Andes, that caps the low-level flow inhibiting the convection close to the Andes, represent the key ingredients for upscaled convective systems developing over SESA. Furthermore, the cyclone formation on the lee side of the Andes is another important feature of convection initiation, enhancing northerly flow and favoring a strong moisture flux convergence that fuels long-lived MSCs over SESA (Rasmussen and Houze, 2016; Salio et al, 2007). Hence, the evolution of MCSs in SESA is highly influenced by the SALLJ and by the low-level circulation pattern. Therefore, we focus on evaluating how the main synoptic forcing mechanisms described above are captured by the set of CP ensembles. Due to the CP ensembles being short-term simulations lasting for 72-hours, it is not expected that the mid and upper-level circulation features diverge from the driving reanalysis, hence, the analysis is focused on the low-level circulation features at 850hPa. As shown in Solman et al (2021), the location of the exit region of the low-level jet and of the moisture flux convergence largely determines the area where the maximum precipitation occurs during the subsequent hours. Hence, Figures 7, 8 and 9 display the 850hPa circulation together with the vertically integrated moisture flux 6 hours before the

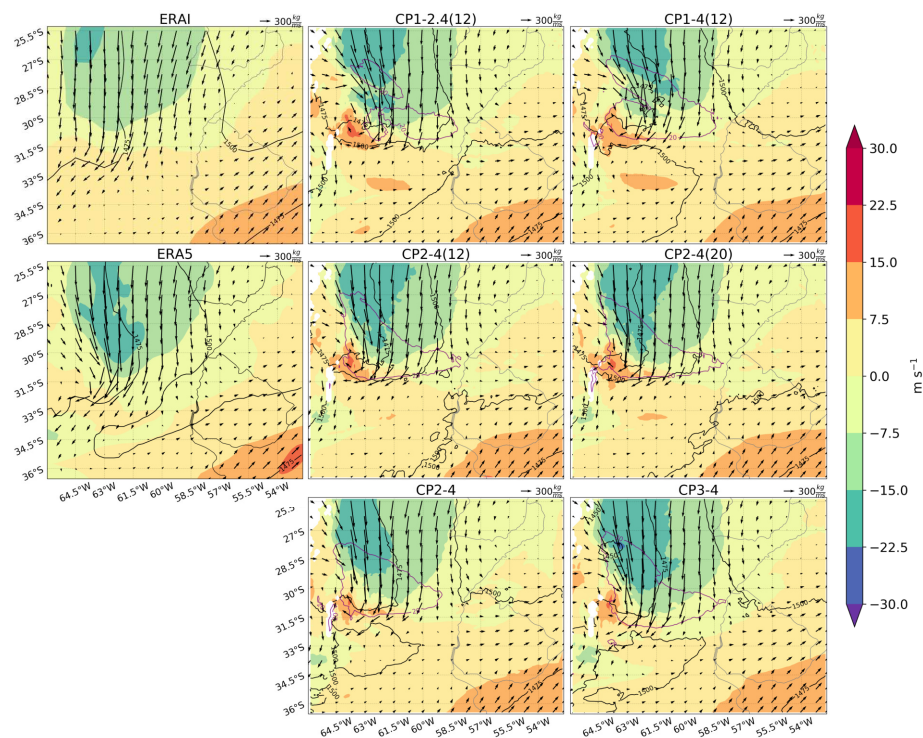


**Fig. 7** Vertically integrated moisture flux (vectors), 850hPa geopotential height (black contours) and intensity of the meridional component of the wind at 850hPa (shaded) 6 hours before the peak precipitation occurs for Case 1. Purple lines display the 20mm contour of the maximum 6-hourly accumulated precipitation. The two top left panels are from ERA-Interim and ERA5, respectively. The rest of the panels display the ensemble mean for each of the 6 CP ensembles.

maximum rainfall rate occurs for Cases 1, 2 and 3, respectively, as depicted by 571  
 the reanalysis and the CP ensemble simulations. It is interesting to highlight that 572  
 for the three events, the ERA5 reanalysis depict important differences compared 573  
 with the ERA-Interim dataset in terms of the intensity and southward penetra- 574  
 tion of the low-level jet and in the spatial configuration of the moisture flux. These 575  
 differences may be associated with the spatial resolution of the two reanalyses 576

For Case 1 (Fig. 7), the ERA5 reanalysis shows a strong southward meridional 577  
 flow with intensities above 15 m/s, which provides the moist and warm conditions 578  
 over the target region. The moisture flux penetrates southward with the area of 579  
 maximum convergence located over the area where the maximum rainfall core is 580  
 observed (Fig. 2), roughly around 31°S 61.5°W. As indicated above, the ERA- 581

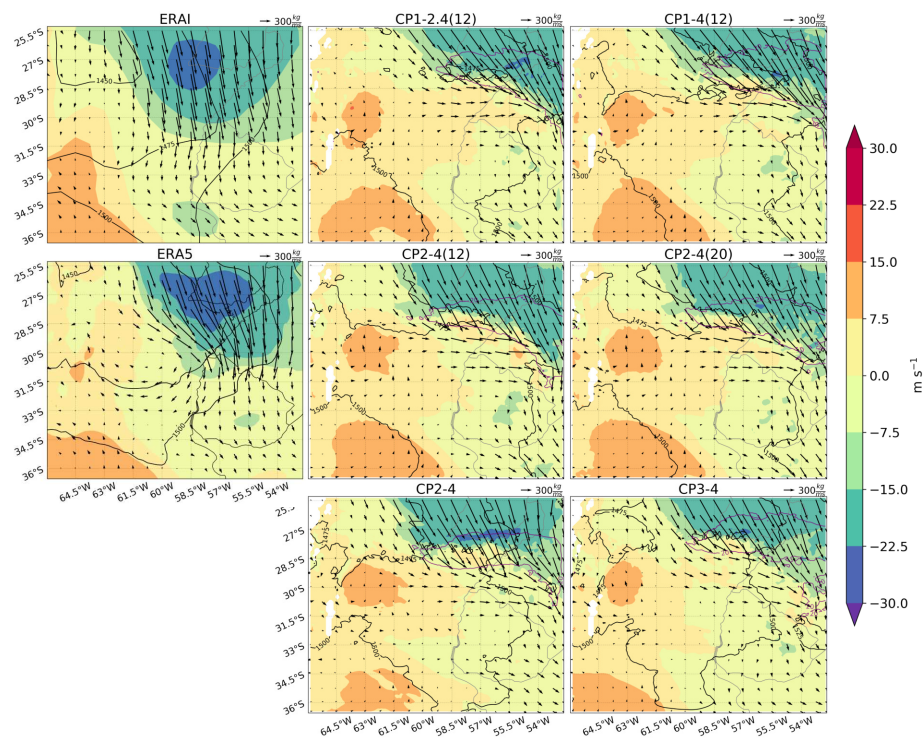


**Fig. 8** Same as Fig. 7 but for Case 2.

582 Interim reanalysis shows a slightly less intense meridional wind and moisture flux.  
 583 The CP ensembles agree better with the ERA5 rather than with the ERA-Interim  
 584 reanalysis, even though these are driven by the latter. This suggests that the  
 585 horizontal resolution may have a role in how the low-level flow is represented,  
 mostly when the flow configuration is modulated by the topography, as occurs here. 586  
 For every CP ensemble, the exit region of the low-level jet is collocated with the 587  
 core of the rainfall event, in agreement with Lavín Gullón et al (2021) and Solman 588  
 et al (2021). Inspection of the same fields in the driving domains (with coarser 589  
 resolution and parameterized convection) reveals that the moisture penetration 590  
 was underestimated, resulting in precipitation patterns located further north with 591  
 respect to the CP simulations and the observations (not shown). The two CP 592  
 ensembles for the D1 domain, CP1-2.4(12) and CP1-4(12), display quite similar 593  
 results. This is expected given that the CP domain extends over a 12°x 13° (lon-lat) 594

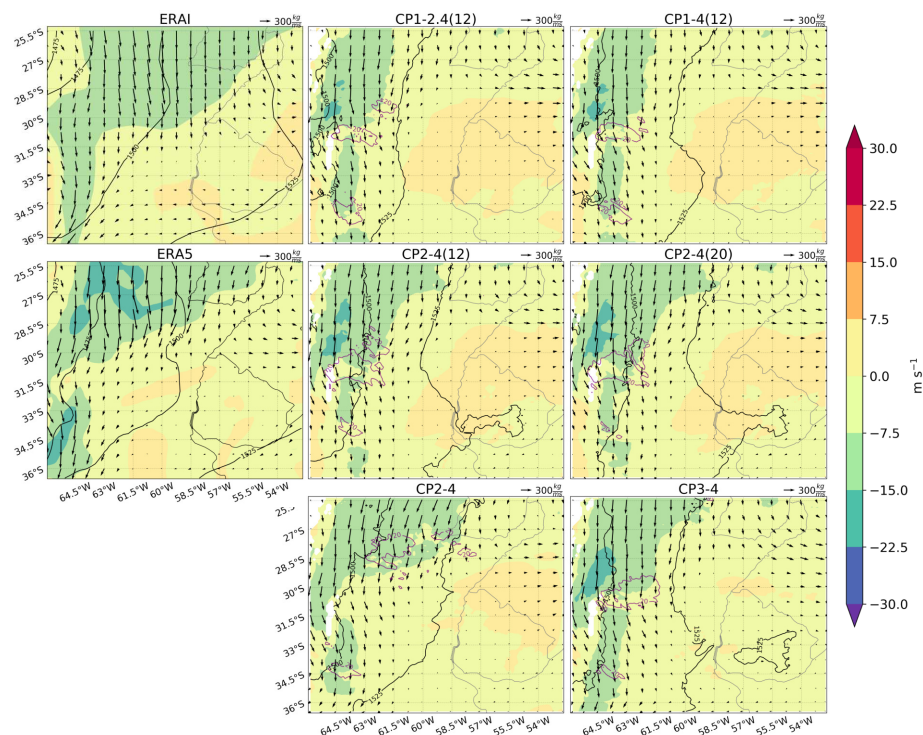


**Fig. 9** Same as Fig. 7 but for Case 3. The maximum precipitation for this event occurs at a time not available for ERA-Interim, hence, the synoptic drivers correspond to 3 hours later than the rest of the panels.

region mostly over a flat area, being the western boundary too close to the Sierras 595  
de Córdoba, hence, the topography either at 2.4km or 4km resolution, is not able 596  
to modulate the flow within the CP domain. Enlarging the CP domain towards the 597  
west (the D2 domain), where the main topographic systems that exert an impact 598  
on the initiation of convection are included, does not display any strong impact 599  
on the simulated circulation either. Similarly, the two two-step nesting simulations 600  
for the D2 domain, CP2-4(12) and CP2-4(20), are very similar, independently of 601  
the resolution of the driving domain. The one-step nesting CP ensembles in any 602  
of the two domains, CP2-4 and CP3-4, display a better agreement with the ERA5 603  
reanalysis in terms of the southward penetration of the low level jet and in the 604  
location of its exit region, being the CP ensemble over the D3 domain (CP3-4) the 605  
one that better captures the moisture flux convergence, the location of the cyclonic 606

circulation close to the western boundary and the location of the exit region of the low level jet. This is consistent with the better agreement with the observations of the CP3-4 ensemble in terms of the location of the core of the rainfall event mentioned previously.

For Case 2 (Figure 8) both, the ERA5 and the ERA-Interim reanalysis display the exit region of the low-level jet and the convergence of the moisture flux over the region where the maximum rainfall is observed (see Fig. 3), with ERA5 depicting more intense meridional wind and moisture flux and the presence of a cyclonic circulation to the west of the rainfall maximum, which is not apparent in the ERA-Interim reanalysis. This circulation is important due to it enhances the northwesterly flow and modulates the moisture flux convergence. Every CP ensemble captures this cyclonic circulation though shifted to the southeast compared with ERA5, affecting where the convergence of the moisture flux occurs and hence where the maximum precipitation is simulated. For all CP ensembles the moisture flux is deflected eastwards and the area of moisture flux convergence is located further to the north compared with ERA5, consistent with the location of the rainfall core. Note also that for domains D1 and D2 the system develops too close to the northern boundary, suggesting again, that these domains may be too small to capture systems developing within SESA. All CP ensemble simulations depict very similar circulation patterns, which explains their agreement in the representation of the extreme rainfall event. The performance of the CP simulations in capturing this event seems to be strongly conditioned by the quality of the driving reanalysis.

For Case 3 (Figure 9) differences between the two reanalyses in terms of both the intensity of the low-level jet and the moisture flux field are remarkable. The location of the core rainfall event (Fig. 4) agrees better with the exit region of the low-level jet and with the region where moisture flux converges in the ERA5 rather than the ERA-Interim reanalysis. Moreover, all CP ensemble simulations agree better with the ERA5 than with the ERA-Interim. For CP ensembles over D1, the

636 area of maximum northerly wind and the area where moisture flux converges is  
637 shifted to the west compared with the ERA5 reanalysis. The misrepresentation of  
638 these key circulation features may explain the misrepresentation of the area where  
639 the rainfall core is simulated. Additionally, no added value is apparent when the  
640 CP simulation is performed at higher resolution. Enlarging the domain of the CP  
641 simulations (CP1-4 (12) vs CP2-4(12)) impacts on the simulated circulation, as  
642 can be seen in the spatial distribution of the intensity of the meridional component  
643 of the wind and in the moisture flux. However, the convergence of the moisture  
flux is also shifted to the west compared with ERA5, which may explain why the 644  
rainfall event is also shifted westwards compared with the observations. As noted 645  
previously when evaluating the simulated precipitation patterns, the differences 646  
between the two two-step nesting CP ensembles for domain D2 are negligible, sug- 647  
gesting that the spatial resolution of the driving domain does not exert a strong 648  
influence on the CP simulation. The one-step nesting CP ensemble for the D2 649  
domain (CP2-4) arises as the simulation that best captures the circulation com- 650  
pared with ERA5. Note that this simulation arose also as the one with the best 651  
performance in reproducing the location of the extreme rainfall event (Fig. 4). 652  
However, the pattern of the moisture flux over the target domain in the CP3-4 653  
ensemble agrees better with the pattern depicted by ERA5 than any other CP 654  
ensemble. This may be related with the extension of the CP3-4 domain, which 655  
allows representing better the inflow over the northern part of the domain, given 656  
that the northern boundary is located at 15°S and hence, it captures the interac- 657  
tion between the northerly flow and the topography over Bolivia and northwestern 658  
Argentina, which deflects the low-level jet towards SESA. 659

Overall, it is apparent that every CP ensemble simulates the core of the rainfall 660  
event at the exit region of the low-level jet, where the moisture flux converges. This 661  
behavior suggests that, if the CP simulation is able to capture the synoptic scale 662  
forcings that provide the environmental conditions for deep moist convection to 663  
develop, they are also able to capture the rainfall event. The CP simulations over 664

the D2 and the D3 domains, either the two-step nesting or the one-step nesting CP ensembles, arise as those with better performance in terms of simulating both the synoptic-scale forcings and the extreme precipitation events, compared with the smaller CP domain (D1).

Concerning the nesting strategy, it is important to recall that multiple nestings may deteriorate the quality of the CP simulations due to errors inherited from one driving domain to another (Brisson et al, 2015), besides of being computationally more expensive. On the other hand, the resolution jump between the model providing the LBCs and the driven CPM, which is close to 18 for the CP2-4 and CP3-4 simulations, determines the spin-up distance within the nested domain, i.e., the extension of the area close to the lateral boundaries that should be discarded. As discussed by Matte and Lucas-Picher (2017), the spatial spin-up depends on the spatial resolution of the LBC. These authors suggested that the larger the resolution jump the larger the number of grid points that should be discarded from the analysis in the nested domain. Hence, considering the tradeoffs between the one-step versus the two-steps nestings, and in order to objectively assess the convenience of one strategy over the other, the RMSE of the geopotential height at 850hPa computed against the reanalysis has been evaluated for the CP ensembles along the length of the simulated period for each case. The RMSE has been computed within the common CP2 domain considering the DR2-12, CP2-4(12), CP2-4 and CP3-4 ensembles against both ERA-Interim and ERA5. A region extending  $2.25^\circ$  away from the boundary of the CP2 domain has been discarded to account for the spatial spin-up. Each simulation has been interpolated to the grid of the reanalysis to which it is being compared ( $0.25^\circ \times 0.25^\circ$  for ERA5 and  $0.75^\circ \times 0.75^\circ$  for ERAI). Similar results were obtained for ERA-Interim, with slightly higher values of RMSE, so Figure 10 displays the RMSE against ERA5 after discarding the temporal spin-up time (6 hours). All CP simulations displays smaller errors compared with the DR2 ensemble simulation, indicating the added value of the CP simulations. However, the one-step nesting simulations depicts smaller RMSEs

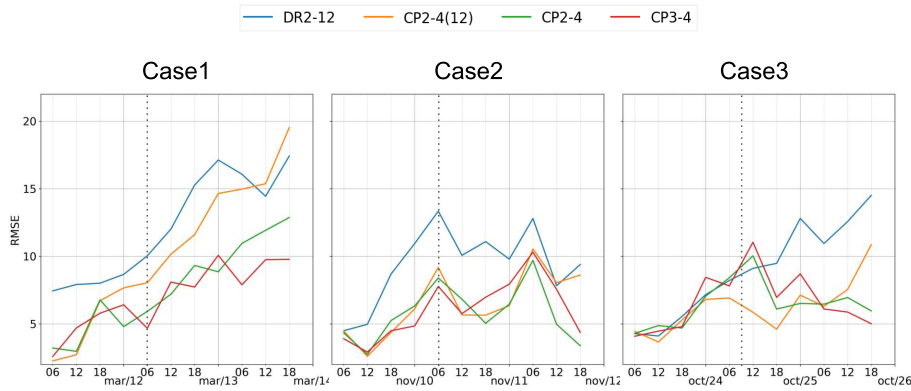


**Fig. 10** Temporal evolution of the RMSE (m) computed for the 850hPa geopotential height against the ERA5 reanalysis for Cases 1, 2 and 3 (left, central and right columns, respectively). Vertical dashed lines denote the time of the maximum rainfall. Blue for DR2-20, orange for CP2-4(20), green for CP2-4 and red for CP3-4.

compared with the two-step nesting CP simulation for Case 1. Case2 shows similar  
 694  
 RMSE for both the one-step and two-step nesting simulations, while Case3 shows  
 695  
 bigger errors at the time of the maximum precipitation for the one-step nesting  
 696  
 simulations. Nevertheless, during the late stages of the events, the RMSE of the  
 697  
 one-step nesting simulations tend to decrease, while the opposite occur for the  
 698  
 two-step nested simulation, reaching values similar to those of the driving simu-  
 699  
 lation. This behavior may have important consequences for longer, climatic scale  
 700  
 CP simulations. This result shows that the one-step nesting CP simulations do not  
 701  
 deteriorate the quality of the simulated fields compared with the two-step nesting,  
 702  
 independently of the size of the CP domain. Regarding the one-step nested simu-  
 703  
 lations, the CP3-4 ensemble displays values of RMSEs similar to the CP2-4. There  
 704  
 is no evidence of systematic improvement for one against the other regarding these  
 705  
 three events. Recall that the larger the domain size (in this case CP3 vs CP2),  
 706  
 the larger the freedom of the CP simulation in developing a circulation that may  
 707  
 differ from the circulation provided at the lateral boundaries of the domain by the  
 708  
 reanalysis so the RMSE suggests that a bigger CP domain did not prejudice the  
 709  
 quality of the simulated circulation. 710

#### 4 Summary and conclusions

711

This study explores a variety of modeling strategies for performing convection-permitting simulations over Southeastern South America. The aim of the study is to identify the most suitable model configuration for reproducing the evolution of extreme rainfall events and their triggering mechanisms at a feasible computational cost. For that purpose, a set of 6 experiments focused on exploring the choice of the nesting strategy, the spatial resolution and the domain size were performed based on short-term simulations lasting 72 hours using the WRF 3.9.1 model for three extreme precipitation events. For each of the selected cases, a 6-member physics ensemble was built in order to account for model uncertainty. All simulations were driven by the ERA-Interim reanalysis dataset.

712

713

714

715

716

717

718  
719  
720  
721

The evaluation of the set of experiments is focused on the temporal evolution and spatial distribution of rainfall against a set of satellite-based precipitation observations. Including a set of observations allows acknowledging the observational uncertainty which is particularly large for extreme events in the target region. Additionally, given the strong control of the synoptic circulation during the early stages of the development of the events, the synoptic forcings were also evaluated against two different reanalyses: ERA-Interim and ERA5. The analysis based on individual events contributes to better understanding the mechanisms that may explain model deficiencies.

722

723

724

725

726

727

728

729

730

Several research questions drove this study. The question concerning the need of improving the resolution of the convection-permitting simulations was addressed by comparing the two-step nesting CP ensemble at 2.4km resolution against a 4km resolution for a CP domain spanning an area of  $13^{\circ} \times 12^{\circ}$  (lon-lat). No significant differences were found between these two sets of experiments in terms of their capability in reproducing the main features of the extreme events together with the structure of the meridional flow at 850hPa, the moisture flux convergence and the low-level circulation patterns. Additionally, the two-step nesting 2.4km resolution CP ensemble required 3,5 times the computational resources of the two-step

731

732

733

734

735

736

737

738

739

740 nesting 4km resolution one over the same CP domain. Hence, considering the bal-  
741 ance between the computational cost and the quality of this pair of simulations,  
742 it is concluded that CP simulations operating at 4km resolution could be consid-  
743 ered as a reasonable resolution choice as no additional added value is apparent  
744 at higher resolution. To explore whether the resolution of the driving domain in  
745 a two-step nesting approach matters, two sets of experiments were compared in  
746 which the resolution of the driving domain was 12 km and 20 km, respectively.  
It was found that increasing the resolution of the driver domain introduces only 747  
subtle differences in the performance of the CP ensembles, shown in terms of the 748  
smaller minimum spatial skillful scales found for the CP2-4(12) compared with 749  
the CP2-4(20) ensembles. This may be due to the fact that no relevant differences 750  
arise when the horizontal resolution of the driving domain increases from 20 to 751  
12km. A significant improvement in the quality of the CP ensemble was found 752  
when enlarging the CP domain size from the  $13^{\circ}\times 12^{\circ}$  (lon-lat) to the  $25^{\circ}\times 16^{\circ}$ , re- 753  
ferred to as CP1-4(12) and CP2-4(12), respectively. The major difference between 754  
these two domains is the position of the western boundary, which is located over 755  
the eastern Pacific Ocean, i.e. shifted to the west in the CP2 domain compared 756  
with the CP1 domain. This improvement is apparent in the simulated precipi- 757  
tation and in the synoptic circulation triggering the extreme events. This result 758  
was expected given the relevant role of the Andes and the Sierras de Cordoba 759  
topographic features in the initiation of convection, given the environmental fa- 760  
vorable conditions that fuels the subsequent eastern progression and upscale of 761  
the systems. Hence, it is recommended that convection-permitting simulation for 762  
SESA should be performed over a domain that extends westwards at least over the 763  
eastern Pacific Ocean to include the topographic forcing which triggers convection 764  
and modulates the synoptic scale circulation. 765

Concerning the nesting strategy, a two-step nesting approach was compared 766  
with a one-step nesting approach in which the CP simulations were driven di- 767  
rectly by the reanalysis. Additionally, the one-step nesting was implemented for 768

two domain sizes, extending over a  $25^{\circ}\times 16^{\circ}$  lon-lat box and over a larger area (769  
( $29^{\circ}\times 21^{\circ}$ ). In the latter, the northern boundary is shifted further to the north (770  
with the aim of including the area where the low-level jet reaches its maximum (771  
intensity within the CP domain. Note also that this larger domain is also enlarged (772  
towards the east, to better capture the incoming flow from the northeastern and (773  
from the Atlantic Ocean which increases the moisture flux towards SESA. The (774  
one-step nesting simulations, for both the CP2 and CP3 domains, showed major (775  
differences against the rest of the CP simulations in terms of the minimum skillful  
776 spatial scales, suggesting that these simulations outperform in the representation  
777 of localized heavy rainfall all along the temporal evolution of the events. Addi-  
778 tionally, these simulations reproduced the synoptic forcings associated with the  
779 events similarly compared with the two-nesting simulation over the  $25^{\circ}\times 16^{\circ}$  do-  
780 main. It was also noted that the spread among ensemble members turned out to  
781 be slightly smaller for the one-nesting approach compared with the two-nesting  
782 approach, as expected, particularly evident after the decay of the extreme event.  
783 This occurs also for the larger CP domain. This feature is particularly important  
784 when considering CP simulations covering longer periods.  
785

786 Focusing specifically on the one-step nesting approach, it is found that enlarg-  
787 ing the CP domain has some benefits and some drawbacks. The larger CP domain  
788 allows the synoptic drivers of the extreme events being better reproduced, given  
789 the importance of the topography in modulating the low-level circulation. On the  
790 other hand, the computational cost of the simulations also increases, and this may  
791 limit the technical capability for performing longer term climatic simulations. It  
792 is worth highlighting that the computational cost of the one-step nesting CP2-4  
793 ensemble resulted 30% less expensive compared with the two-step nesting CP2-  
794 4(12). Additionally, the one-step nesting CP3-4 ensemble yielded a computational  
795 cost similar to that of two-step nesting CP2-4(12) ensemble, but with a consider-  
796 ably larger CP domain. Moreover, it is demonstrated that for the three individual  
797 events evaluated in this work, the one-step nesting CP simulations do not dete-

riorate the quality of the simulated fields compared with the two-step nesting,  
independently of the size of the CP domain. This behavior may have important  
consequences for longer, climatic scale CP simulations. A major drawback in the  
one-step nesting approach is the resolution jump between the model providing the  
LBC and the CPM. Brisson et al (2015) suggested that the larger the resolution  
jump the larger the area close to the boundaries that should be discarded due  
to the spatial spin-up. Moreover, given that multiple nestings increases the biases  
that are transferred from one domain to another, the one-step nesting approach  
may prevent this major shortcoming.

Given the multiple evidence of the advantages and limitations of the various CP  
configurations discussed in this study, we consider the one-step nesting approach  
operating at 4 km over the D3 domain as the recommended CPM configuration  
for SESA. We are aware, however, that the simulations evaluated here last 72-  
hours and hence are strongly controlled by the initial conditions. Though the  
behavior of longer-term simulations covering various months or years cannot be  
directly extrapolated from this exercise, the results described in this work can be  
considered as a guidance for planning long-term climatic simulations over SESA  
with CPM ensembles.

## References

- Ban N, Schmidli J, Schär C (2015) Heavy precipitation in a changing climate: Does  
short-term summer precipitation increase faster? *Geophysical Research Letters*  
42, DOI <https://doi.org/10.1002/2014GL062588>
- Ban N, Rajczak J, Schmidli J, Schär C (2020) Analysis of alpine precipitation  
extremes using generalized extreme value theory in convection-resolving climate  
simulations. *Climate Dynamics* 55, DOI <https://doi.org/10.1007/s00382-018-4339-4>
- Ban N, Caillaud C, Coppola E, Pichelli E, Sobolowski S, Adinolfi M, Ahrens  
B, Alias A, Anders I, Bastin S, Belušić D, Berthou S, Brisson E, Cardoso

R, Chan S, Christensen O, Fernández J, Fita L, Frisius T, Zander M (2021) 826  
The first multi-model ensemble of regional climate simulations at kilometer- 827  
scale resolution, part i: evaluation of precipitation. *Climate Dynamics* DOI 828  
<https://doi.org/10.1007/s00382-021-05708-w> 829

Beck H, Vergopolan N, Pan M, Levizzani V, van Dijk A, Weedon G, Brocca L, Pap- 830  
penberger F, Huffman G, Wood E (2017) Global-scale evaluation of 22 precipi- 831  
tation datasets using gauge observations and hydrological modeling. *Hydrology* 832  
and *Earth System Sciences* 21:6201–6217, DOI [https://doi.org/10.5194/hess-21-](https://doi.org/10.5194/hess-21-6201-2017)  
6201-2017 834

Beck H, Wood E, Pan M, Fisher C, Miralles D, van Dijk A, McVicar T, Adler R 835  
(2018) MSWEP v2 global 3-hourly 0.1° precipitation: Methodology and quan- 836  
titative assessment. *Bulletin of the American Meteorological Society* 100, DOI 837  
<https://doi.org/10.1175/BAMS-D-17-0138.1> 838

Berthou S, Kendon E, Chan S, Ban N, Leutwyler D, Schär C, Fosser G (2020) 839  
Pan-european climate at convection-permitting scale: a model intercomparison 840  
study. *Climate Dynamics* 55, DOI <https://doi.org/10.1007/s00382-018-4114-6>

Bettolli M, Solman S, Rocha R, Llopart M, Gutierrez J, Fernández J, Olmo 841  
M, Lavín Gullón A, Chou S, Carneiro Rodrigues D, Coppola E, Balmaceda- 842  
Huarte R, Barreiro M, Blazquez J, Doyle M, Feijoó M, Huth R, Machado L, 843  
Vianna Cuadra S (2021) The CORDEX Flagship Pilot Study in southeastern 844  
South America: a comparative study of statistical and dynamical downscaling 845  
models in simulating daily extreme precipitation events. *Climate Dynamics* 56:3, 846  
DOI <https://doi.org/10.1007/s00382-020-05549-z> 847  
848

Blazquez J, Solman S (2020) Multiscale precipitation variability and ex- 849  
tremes over South America: analysis of future changes from a set of 850  
CORDEX regional climate model simulations. *Climate Dynamics* 55, DOI 851  
<https://doi.org/10.1007/s00382-020-05370-8> 852

Brisson E, Demuzere M, Nicole V (2015) Modelling strategies for performing con- 853  
vective permitting climate simulations. *Meteorologische Zeitschrift* 25, DOI 854

855 <https://doi.org/10.1127/metz/2015/0598>

856 Cerón W, Kayano M, Andreoli R, Avila-Diaz A, Ayes I, Freitas E, Martins J,  
857 Souza R (2020) Recent intensification of extreme precipitation events in the  
858 La Plata Basin in Southern South America (1981–2018). *Atmospheric Research*  
859 DOI <https://doi.org/10.1016/j.atmosres.2020.105299>

860 Chou SC, Lyra A, Mourão C, Dereczynski C, Pilotto I, Gomes J, Bustamante J,  
Tavares P, Silva A, Rodrigues D, Campos D, Chagas D, Medeiros G, Siqueira  
861 G, Marengo J (2014) Assessment of climate change over South America under  
862 RCP 4.5 and 8.5 downscaling scenarios. *American Journal of Climate Change*  
863 03:512–527, DOI <https://doi.org/10.4236/ajcc.2014.35043> 864

Coppola E, Sobolowski S, Pichelli E, Raffaele F, Ahrens B, Anders I, Ban N,  
865 Bastin S, Belda M, Belusic D, Caldas-Alvarez A, Cardoso R, Davolio S, Dobler  
866 A, Fernández J, Fita L, Fumiere Q, Giorgi F, Goergen K, Warrach-Sagi K (2020)  
867 A first-of-its-kind multi-model convection permitting ensemble for investigating  
868 convective phenomena over Europe and the Mediterranean. *Climate Dynamics*  
869 55, DOI <https://doi.org/10.1007/s00382-018-4521-8> 870

Cui W, Dong X, Xi B, Feng Z, Fan J (2019) Can the GPM IMERG Fi-  
871 nal Product accurately represent MCSs' precipitation characteristics over the  
872 central and eastern United States? *Journal of Hydrometeorology* 21, DOI  
873 <https://doi.org/10.1175/JHM-D-19-0123.1> 874

Dee D, Uppala SM, Simmons AJ, Berrisford P, Poli P, Kobayashi S, Andrae U,  
875 Balmaseda M, Balsamo G, Bauer P, Bechtold P, Beljaars ACM, van de Berg L,  
876 Bidlot J, Bormann N, Delsol C, Dragani R, Fuentes M, Geer AJ, Haimberger L,  
877 Healy S, Hersbach H, Hólm EV, Isaksen L, Kallberg P, Kohler M, Matricardi M,  
878 McNally AP, Monge-Sanz BM, Morchette J, Park BK, Peubey C, de Rosnay P,  
879 Tavolato C, Thépaut JN, Vitart F (2011) The ERA-Interim reanalysis: Configu-  
880 ration and performance of the data assimilation system. *Quarterly Journal of the*  
881 *Royal Meteorological Society* 137:553–597, DOI <https://doi.org/10.1002/qj.828> 882

- Demaria E, Rodriguez D, Ebert E, Salio P, Su F, Valdes J (2011) Evaluation of  
mesoscale convective systems in South America using multiple satellite products  
and an object-based approach. *Journal of Geophysical Research-Atmospheres*  
116, DOI <https://doi.org/10.1029/2010jd015157>
- Dudhia J (1989) Numerical study of convection observed during the winter  
monsoon experiment using a mesoscale two-dimensional model. *Journal of*  
*The Atmospheric Sciences* 46:3077–3107, DOI [https://doi.org/10.1175/1520-0469\(1989\)046<3077:NSOCOD>2.0.CO;2](https://doi.org/10.1175/1520-0469(1989)046<3077:NSOCOD>2.0.CO;2)
- Falco M, Carril A, Menéndez C, Zaninelli P, Li L (2019) Assessment of CORDEX  
simulations over South America: added value on seasonal climatology and resolu-  
tion considerations. *Climate Dynamics* 52, DOI <https://doi.org/10.1007/s00382-018-4412-z>
- Fantini A, Raffaele F, Torma C, Bacer S, Coppola E, Giorgi F, Ahrens B, Dubois  
C, Sanchez E, Verdecchia M (2018) Assessment of multiple daily precipita-  
tion statistics in ERA-Interim driven Med-CORDEX and EURO-CORDEX ex-  
periments against high resolution observations. *Climate Dynamics* 51, DOI  
<https://doi.org/10.1007/s00382-016-3453-4>
- Fosser G, Khodayar Pardo S, Berg P (2014) Benefit of convection permitting  
climate model simulations in the representation of convective precipitation. *Cli-  
mate Dynamics* 44:45–60, DOI <https://doi.org/10.1007/s00382-014-2242-1>
- Fosser G, Khodayar S, Berg P (2016) Climate change in the next 30 years: What  
can a convection-permitting model tell us that we did not already know? *Climate*  
*Dynamics* DOI <https://doi.org/10.1007/s00382-016-3186-4>
- Grell G, Freitas S (2014) A scale and aerosol aware stochastic convective param-  
eterization for weather and air quality modeling. *Atmospheric Chemistry and*  
*Physics Discussions* 13, DOI <https://doi.org/10.5194/acp-14-5233-2014>
- Hersbach H, Bell B, Berrisford P, Horányi A, Sabater JM, Nicolas J,  
Radu R, Schepers D, Simmons A, Soci C, Dee D (2019) Global reanal-  
ysis: goodbye ERA-Interim, hello ERA5. *ECMWF Newsletter* 156, DOI

- 912 <https://doi.org/10.21957/vf291hehd7>
- 913 Hersbach H, Bell B, Berrisford P, Hirahara S, Horányi A, Muñoz Sabater J, Nicolas  
914 J, Peubey C, Radu R, Schepers D, Simmons A, Soci C, Abdalla S, Abellan X,  
915 Balsamo G, Bechtold P, Biavati G, Bidlot J, Bonavita M, Thépaut JN (2020)  
916 The ERA5 global reanalysis. *Quarterly Journal of the Royal Meteorological*  
917 *Society* DOI <https://doi.org/10.1002/qj.3803>
- 918 Hibino K, Takayabu I, Wakazuki Y, Ogata T (2018) Physical re-  
sponses of convective heavy rainfall to future warming condition: Case  
study of the Hiroshima event. *Frontiers in Earth Science* 6, DOI  
<https://doi.org/10.3389/feart.2018.00035>
- Hong SY, Jang J (2018) Impacts of shallow convection processes on a simulated  
boreal summer climatology in a global atmospheric model. *Asia-Pacific Journal*  
of Atmospheric Sciences 54:361–370, DOI [https://doi.org/10.1007/s13143-018-](https://doi.org/10.1007/s13143-018-0013-3)  
0013-3
- Hong SY, Noh Y, Dudhia J (2006) A new vertical diffusion package with an ex-  
plicit treatment of entrainment processes. *Monthly Weather Review* 134, DOI  
<https://doi.org/10.1175/MWR3199.1>
- Huffman G, Bolvin D, Nelkin E, Adler R (2011) Highlights of Version 7 TRMM  
Multi-satellite Precipitation Analysis (TMPA). 5th Internat Precip Working  
Group Workshop, Workshop Program and Proceedings pp 109–110
- Huffman G, Stocker E, Bolvin D, Nelkin E, Jackson T (2019) GPM IMERG Final  
Precipitation L3 Half Hourly 0.1 degree x 0.1 degree V06, Greenbelt, MD, God-  
dard Earth Sciences Data and Information Services Center (GES DISC). URL  
<https://doi.org/10.5067/GPM/IMERG/3B-HH/06>
- Janjic Z (1994) The step-mountain eta coordinate model: Further develop-  
ment of the convection, viscous sublayer, and turbulent closure schemes.  
*Monthly Weather Review* 122:927–945, DOI [https://doi.org/10.1175/1520-](https://doi.org/10.1175/1520-0493(1994)122<0927:TSMECM>2.0.CO;2)  
0493(1994)122<0927:TSMECM>2.0.CO;2

- Janjic Z (2002) Nonsingular implementation of the Mellor–Yamada Level 2.5  
scheme in the NCEP meso model. NCEP Office Note 436
- Jimenez P, Dudhia J, González Rouco JF, Navarro J, Montávez J, Garcia Bus-  
tamante E (2012) A revised scheme for the WRF surface layer formula-  
tion. *Monthly Weather Review* 140, DOI <https://doi.org/10.1175/MWR-D-11-00056.1>
- Joyce R, Janowiak J, Arkin P, Xie P (2004) CMORPH: A method that pro-  
duces global precipitation estimates from passive microwave and infrared data  
at high spatial and temporal resolution. *Journal of Hydrometeorology* 5, DOI  
[https://doi.org/10.1175/1525-7541\(2004\)005<0487:CAMTPG>2.0.CO;2](https://doi.org/10.1175/1525-7541(2004)005<0487:CAMTPG>2.0.CO;2)
- Kain J (2004) The Kain-Fritsch convective parameterization: An update. *Jour-  
nal of Applied Meteorology* 43:170–181, DOI [https://doi.org/10.1175/1520-0450\(2004\)04360;0170:tkcpau62;2.0.co;2](https://doi.org/10.1175/1520-0450(2004)04360;0170:tkcpau62;2.0.co;2)
- Kendon E, Roberts NM, Senior CA, Roberts MJ (2012) Realism of rainfall in a  
very high-resolution regional climate model. *Journal of Climate* 25(17):5791–  
5806, DOI <https://doi.org/10.1175/JCLI-D-11-00562.1>
- Kendon E, Roberts N, Fowler H, Roberts M, Chan S, Senior C (2014)  
Heavier summer downpours with climate change revealed by weather  
forecast resolution model. *Nature Climate Change* 4:570–576, DOI  
<https://doi.org/10.1038/nclimate2258>
- Kendon E, Ban N, Roberts N, Fowler H, Roberts M, Chan S, Evans J, Fosser G,  
Wilkinson J (2016) Do convection-permitting regional climate models improve  
projections of future precipitation change? *Bulletin of the American Meteor-  
ological Society* 98, DOI <https://doi.org/10.1175/BAMS-D-15-0004.1>
- Lavín Gullón A, Feijoó M, Solman S, Fernández J, Rocha R, Bettolli M (2021)  
Synoptic forcing associated with extreme precipitation events over Southeastern  
South America as depicted by a CORDEX FPS set of convection-permitting  
RCMs. *Climate Dynamics* 56, DOI <https://doi.org/10.1007/s00382-021-05637-8>

- 968 Li J, Chen H, Rong X, Su J, Xin Y, Furtado K, Milton S, Li N (2018) How  
969 well can a climate model simulate an extreme precipitation event: A case  
970 study using the Transpose-AMIP experiment. *Journal of Climate* 31, DOI  
971 <https://doi.org/10.1175/JCLI-D-17-0801.1>
- 972 Li P, Guo Z, Furtado K, Chen H, Li J, Milton S, Field P, Zhou T (2019) Prediction  
973 of heavy precipitation in the eastern China flooding events of 2016: Added value  
974 of convection-permitting simulations. *Quarterly Journal of the Royal Meteorological Society* 145, DOI <https://doi.org/10.1002/qj.3621>
- 976 Lim KS, Hong SY (2010) Development of an effective Double-Moment Cloud  
Microphysics scheme with prognostic cloud condensation nuclei (CCN) for  
977 weather and climate models. *Monthly Weather Review* 138:1587–1612, DOI  
978 <https://doi.org/10.1175/2009MWR2968.1> 979
- Liu C, Ikeda K, Rasmussen R, Barlage M, Newman A, Prein A, Chen L, Clark  
980 M, Dai A, Dudhia J, Eidhammer T, Gochis D, Gutmann E, Kurkute S, Li Y,  
981 Thompson G, Yates D (2017) Continental-scale convection-permitting modeling  
982 of the current and future climate of North America. *Climate Dynamics* 49, DOI  
983 <https://doi.org/10.1007/s00382-016-3327-9> 984
- Mahoney K, Thompson G, Barsugli JJ, Scott JD, Alexander M (2012) Changes  
985 in hail and flood risk in high-resolution simulations over Colorado’s mountains.  
986 *Nature Climate Change* 2, DOI <https://doi.org/10.1038/nclimate1344> 987
- Matsudo C, Salio P (2011) Severe weather reports and proximity to deep con-  
988 vection over Northern Argentina. *Atmospheric Research* 100:523–537, DOI  
989 <https://doi.org/10.1016/j.atmosres.2010.11.004> 990
- Matsudo C, García Skabar Y, Ruiz J, Vidal L, Salio P (2015) Verification of WRF-  
991 ARW convective-resolving forecasts over Southeastern South America. *Mausam*  
992 66:445–456 993
- Matsui T, Zhang S, Lang S, Tao WK, Ichoku C, Peters-Lidard C (2020) Impact  
994 of radiation frequency, precipitation radiative forcing, and radiation column ag-  
995 gregation on convection-permitting West African monsoon simulations. *Climate* 996

Dynamics 55, DOI <https://doi.org/10.1007/s00382-018-4187-2> 997

Matte D, Lucas-Picher P (2017) Spatial spin-up of fine scales in a regional climate model simulation driven by low-resolution boundary conditions. *Climate Dynamics* 49:1–12, DOI <https://doi.org/10.1007/s00382-016-3358-2> 998  
999  
1000

Mlawer E, Taubman S, Brown P, Iacono M, Clough S (1997) Radiative transfer for inhomogeneous atmospheres: RRTM, a validated correlated-k model for the longwave. *Journal of Geophysical Research* 102:16663–16682, DOI <https://doi.org/10.1029/97JD00237> 1001  
1002  
1003  
1004

Nakanishi M, Niino H (2009) Development of an improved turbulence closure model for the atmospheric boundary layer. *Journal of the Meteorological Society of Japan* 87:895–912, DOI <https://doi.org/10.2151/jmsj.87.895> 1005  
1006  
1007

Olmo M, Bettolli M (2021) Extreme daily precipitation in southern South America: statistical characterization and circulation types using observational datasets and regional climate models. *Climate Dynamics* DOI <https://doi.org/10.1007/s00382-021-05748-2> 1008  
1009  
1010  
1011

Olmo M, Bettolli M, Rusticucci M (2020) Atmospheric circulation influence on temperature and precipitation individual and compound daily extreme events: Spatial variability and trends over southern South America. *Weather and Climate Extremes* 29:100267, DOI <https://doi.org/10.1016/j.wace.2020.100267> 1012  
1013  
1014  
1015

Pall P, Patricola C, Wehner M, Stone D, Paciorek C, Collins W (2017) Diagnosing conditional anthropogenic contributions to heavy Colorado rainfall in September 2013. *Weather and Climate Extremes* 17, DOI <https://doi.org/10.1016/j.wace.2017.03.004> 1016  
1017  
1018  
1019

Penalba O, Robledo F (2010) Spatial and temporal variability of the frequency of extreme daily rainfall regime in the La Plata Basin during the 20th century. *Climatic Change* 98:531–550, DOI <https://doi.org/10.1007/s10584-009-9744-6> 1020  
1021  
1022

Pichelli E, Coppola E, Sobolowski S, Ban N, Giorgi F, Stocchi P, Alias A, Belušić D, Berthou S, Caillaud C, Cardoso R, Chan S, Christensen O, Dobler A, de Vries H, Goergen K, Kendon E, Keuler K, Lenderink G, Vergara-Temprado J (2021) 1023  
1024  
1025

- 1026 The first multi-model ensemble of regional climate simulations at kilometer-scale  
1027 resolution part 2: historical and future simulations of precipitation. *Climate*  
1028 *Dynamics* 56, DOI <https://doi.org/10.1007/s00382-021-05657-4>
- 1029 Prein A, Gobiet A, Suklitsch M, Truhetz H, Awan N, Keuler K, Georgievski G  
1030 (2013) Added value of convection permitting seasonal simulations. *Climate Dy-*  
1031 *namics* 41, DOI <https://doi.org/10.1007/s00382-013-1744-6>
- 1032 Prein A, Langhans W, Fosser G, Ferrone A, Ban N, Goergen K, Keller M, Tölle  
1033 M, Gutjahr O, Feser F, Brisson E, Kollet S, Schmidli J, P M van Lipzig N,  
1034 Leung L (2015) A review on regional convection-permitting climate modeling:  
Demonstrations, prospects, and challenges. *Reviews of Geophysics* 53, DOI 1035  
<https://doi.org/10.1002/2014RG000475> 1036
- Prein A, Liu C, Ikeda K, Bullock R, Rasmussen R, Holland G, Clark 1037  
M (2020a) Simulating North American mesoscale convective systems with 1038  
a convection-permitting climate model. *Climate Dynamics* 55, DOI 1039  
<https://doi.org/10.1007/s00382-017-3993-2> 1040
- Prein A, Rasmussen R, Castro C, Dai A, Minder J (2020b) Special issue: Ad- 1041  
vances in convection-permitting climate modeling. *Climate Dynamics* 55, DOI 1042  
<https://doi.org/10.1007/s00382-020-05240-3> 1043
- Rasmussen K, Houze R (2016) Convective initiation near the Andes 1044  
in subtropical South America. *Monthly Weather Review* 144, DOI 1045  
<https://doi.org/10.1175/MWR-D-15-0058.1> 1046
- Rasmussen K, Chaplin MM, Zuluaga MD, Houze RA (2016) Contribution of ex- 1047  
treme convective storms to rainfall in South America. *Journal of Hydrometeo-*  
1048 *rology* 17(1):353–367, DOI <https://doi.org/10.1175/JHM-D-15-0067.1> 1049
- Rasmussen K, Prein A, Rasmussen R, Ikeda K, Liu C (2020) Changes in the con- 1050  
vective population and thermodynamic environments in convection-permitting 1051  
regional climate simulations over the United States. *Climate Dynamics* 55, DOI 1052  
<https://doi.org/10.1007/s00382-017-4000-7> 1053

- Roberts NM, Lean HW (2008) Scale-selective verification of rainfall accumulations  
from high-resolution forecasts of convective events. *Monthly Weather Review*  
136(1):78–97, DOI <https://doi.org/10.1175/2007MWR2123.1>
- Romatschke U, Houze R (2013) Characteristics of precipitating convective systems  
accounting for the summer rainfall of tropical and subtropical South America.  
*Journal of Hydrometeorology* 14:25–46, DOI <https://doi.org/10.1175/JHM-D-12-060.1>
- Salio P, Nicolini M, Zipser E (2007) Mesoscale convective systems over southeast-  
ern south america and their relationship with the South American Low-Level  
Jet. *Monthly Weather Review* 135, DOI <https://doi.org/10.1175/MWR3305.1>
- Salio P, Hobouchian M, García Skabar Y, Vila D (2014) Evaluation of  
high-resolution satellite precipitation estimates over southern South Amer-  
ica using a dense rain gauge network. *Atmospheric Research* 163, DOI  
<https://doi.org/10.1016/j.atmosres.2014.11.017>
- Skamarock W, Klemp J, Dudhia J, O Gill D, Barker D, Wang W, G Powers J  
(2008) A description of the Advanced Research WRF Version 3. NCAR Tech-  
nical Note NCAR/TN-468+STR, DOI <https://doi.org/10.5065/D68S4MVH>
- Solman S (2016) Systematic temperature and precipitation biases in the  
CLARIS-LPB ensemble simulations over South America and possible im-  
plications for climate change projections. *Climate Research* 68, DOI  
<https://doi.org/10.3354/cr01362>
- Solman S, Blazquez J (2019) Multiscale precipitation variability over South Amer-  
ica: Analysis of the added value of CORDEX RCM simulations. *Climate Dy-  
namics* DOI <https://doi.org/10.1007/s00382-019-04689-1>
- Solman S, Sanchez E, Samuelsson P, da Rocha RP, Li L, Marengo J, Pessag  
N, Remedio AR, Chou SC, Berbery H, Le Treut H, de Castro M, Jacob D  
(2013) Evaluation of an ensemble of regional climate model simulations over  
South America driven by the ERA-Interim reanalysis: Model performance and  
uncertainties. *Climate Dynamics* 41, DOI <https://doi.org/10.1007/s00382-013->

1083 1667-2

- 1084 Solman S, Bettolli M, Doyle M, Olmo M, Feijó M, Martínez D,  
1085 Blazquez J, Balmaceda-Huarte R (2021) Evaluation of multiple downscal-  
ing tools for simulating extreme precipitation events over Southeastern 1086  
South America: a case study approach. *Climate Dynamics* pp 1–24, DOI 1087  
<https://doi.org/10.1007/s00382-021-05770-4> 1088
- Tewari M, Wang W, Dudhia J, LeMone M, Mitchell K, Ek M, Gayno G, Wegiel 1089  
J, Cuenca R (2016) Implementation and verification of the united NOAA land 1090  
surface model in the wrf model. pp 11–15 1091
- Torma C, Giorgi F, Coppola E (2015) Added value of regional climate mod- 1092  
eling over areas characterized by complex terrain-precipitation over the 1093  
Alps. *Journal of Geophysical Research: Atmospheres* 120(9):3957–3972, DOI 1094  
<https://doi.org/10.1002/2014JD022781> 1095
- Vörösmarty C, Bravo de Guenni L, Wollheim W, Pellerin B, Bjerklie D, Cardoso 1096  
M, D’Almeida C, Green P, Colon L (2013) Extreme rainfall, vulnerability and 1097  
risk: A continental-scale assessment for South America. *Philosophical transac-* 1098  
*tions Series A, Mathematical, physical, and engineering sciences* 371:20120408, 1099  
DOI <https://doi.org/10.1098/rsta.2012.0408> 1100
- Yang Q, Houze R, Leung L, Feng Z (2017) Environments of long-lived mesoscale 1101  
convective systems over the central United States in convection permitting cli- 1102  
mate simulations. *Journal of Geophysical Research: Atmospheres* 122, DOI 1103  
<https://doi.org/10.1002/2017jd027033> 1104
- Yun Y, Liu C, Luo Y, Liang X, Huang L, Chen F, Rasmussen R (2020) 1105  
Convection-permitting regional climate simulation of warm-season precipitation 1106  
over eastern China. *Climate Dynamics* 54, DOI [https://doi.org/10.1007/s00382-](https://doi.org/10.1007/s00382-019-05070-y) 1107  
[019-05070-y](https://doi.org/10.1007/s00382-019-05070-y) 1108
- Zipser E, J Cecil D, Liu C, Nesbitt S, Yorty D (2006) Where are the most intense 1109  
thunderstorms on Earth? *Bulletin of The American Meteorological Society* 87, 1110  
DOI <https://doi.org/10.1175/BAMS-87-8-1057> 1111